



Metasomatic origin of clinopyroxene in Archean mantle xenoliths from Hebi, North China Craton: Trace-element and Sr-isotope constraints

Jing Sun, Chuan-Zhou Liu*, Fu-Yuan Wu, Yue-Heng Yang, Zhu-Yin Chu

State Key Laboratory of Lithospheric Evolution, Institute of Geology and Geophysics, Chinese Academy of Sciences, Beijing, 100029, China

ARTICLE INFO

Article history:

Accepted 15 March 2012

Available online 23 March 2012

Keywords:

Metasomatism
Mantle xenoliths
Sr isotopes
Re–Os isotopes
Hebi
North China Craton

ABSTRACT

Clinopyroxene is a major host for lithophile elements in the mantle lithosphere, and therefore its origin is critical for constraints on mantle evolution and melt generation. This study presents detailed in-situ trace-element and Sr-isotope analyses of clinopyroxene in the mantle xenoliths from Hebi, North China Craton (NCC). The Archean lithospheric mantle beneath the NCC has been heterogeneously thinned and replaced by juvenile asthenospheric mantle. The Hebi mantle xenoliths mainly consist of spinel harzburgites with highly refractory compositions; most olivines are Fo_{91.1–92.5}. Eight samples have ¹⁸⁷Os/¹⁸⁸Os ratios of 0.11067–0.11688, giving Paleoproterozoic–Archean model ages (*T*_{MA}; 2.3–3.4 Ma) calculated relative to the primitive upper mantle (PUM). This confirms the existence of Archean mantle relics beneath the Hebi area during the Cenozoic. Clinopyroxene in the Hebi mantle xenoliths shows strong enrichment in LILEs (e.g., Th, U and LREE), but depletion in both HREE and HFSEs (e.g., Nb, Ta, Zr and Hf), which suggests that the Hebi mantle xenoliths have been metasomatized by carbonatitic melts. Strontium isotopes in clinopyroxene have been determined in-situ in 13 samples, giving ⁸⁷Sr/⁸⁸Sr ratios of 0.70309–0.70556, which are lower than the bulk-rock values of the Paleozoic mantle xenoliths. Therefore, we suggest that clinopyroxenes in the Hebi mantle xenoliths crystallized from metasomatic melts. However, the metasomatic process has not significantly disturbed the Os isotope ages of the Hebi mantle xenoliths.

© 2012 Elsevier B.V. All rights reserved.

1. Introduction

After its formation, the composition of the lithospheric mantle has been subjected to secular modification by various metasomatic agents. Modal metasomatism can add exotic mineral phases to the lithospheric mantle, such as amphibole and apatite (Menzies and Hawkesworth, 1987). The more modally abundant mantle minerals olivine, orthopyroxene, clinopyroxene and spinel are commonly thought to be generally of primary origin, residual after melt extraction and lithosphere stabilisation. Clinopyroxene is the major host for incompatible elements, such as Sr and REE, in the lithospheric mantle and exerts a dominant control on the long-term evolution of lithophile isotopes such as Rb–Sr, Sm–Nd and Lu–Hf. Its compositions have been widely used to study the complicated processes that have affected the lithospheric mantle. However, a number of studies have demonstrated that clinopyroxene in mantle xenoliths is not necessarily of primary or residual origin (van Achterbergh et al., 2001; Gregoire et al., 2003; Simon et al., 2003, 2007). Mantle xenoliths can show two

generations of clinopyroxene, and the second-generation clinopyroxene can occur as a minor phase on primary rims or along grain boundaries; such clinopyroxene is usually related to infiltration of the host magmas (Pearson et al., 2003). The contribution of secondary clinopyroxene to bulk rock sodium, calcium or iron contents can be considerable (Boyd et al., 1997). Furthermore, several studies have shown that most of the clinopyroxene found in mantle xenoliths from on-craton settings may have a metasomatic origin (van Achterbergh et al., 2001; Gregoire et al., 2003; Pearson et al., 2003; Simon et al., 2003, 2007). Using the micro-drilling technique, Malarkey et al. (2011) have measured both trace elements and Sr–Nd isotopes of clinopyroxenes in off-craton mantle xenoliths from Morocco. They suggested that clinopyroxenes in these xenoliths have a metasomatic rather than residual origin and crystallized during a carbonatitic metasomatic event.

Hebi is located in the central part of the North China Craton (NCC). Previous studies have shown that this Cenozoic xenolith suite contains samples of refractory lithospheric mantle, with ancient sulfide phases (Zheng et al., 2001, 2007). In this study, the whole-rock Re–Os isotope analyses of these xenoliths suggest that they represent Archean cratonic mantle beneath the NCC. In addition, we use laser-ablation method to investigate the trace-element patterns and Sr-isotope ratios of clinopyroxene, and to explore the origin of the clinopyroxene in the Hebi mantle xenoliths.

* Corresponding author. Tel.: +86 10 82998547; fax: +86 10 62010846.
E-mail address: chzliu@mail.iggcas.ac.cn (C.-Z. Liu).

2. Geological background and sample description

2.1. Geological background

The Archean North China Craton (NCC) is bounded by the Xing'an-Mongolian orogenic belt to the north and the Dabie–Sulu ultra-high pressure belt to the south (Fig. 1). The NCC has been divided into eastern and western blocks (Zhao et al., 2001), separated by the Trans-North China Orogen (TNCO). The eastern NCC is characterized by a thin crust and lithospheric mantle, high heat flow and weak negative to positive regional Bouguer anomalies, whereas the western NCC has a relatively thick crust and lithospheric mantle, low heat flow and strong negative Bouguer gravity anomalies (Xu, 2007). The North South Gravity Lineament (NSGL) marks the sharp gradient in Bouguer gravity anomalies; it roughly overlaps the TNCO. Diamond inclusions, xenoliths and mineral concentrates from Paleozoic kimberlites (e.g., Mengyin, Fuxian and Tieling) indicate a thick (>180 km), cold (<40 mW/m²) and refractory lithospheric keel beneath at least the eastern part of the NCC during the Paleozoic (Griffin et al., 1998; Zheng, 1999; Zheng and Lu, 1999). Re–Os isotope data of the mantle xenoliths from the kimberlites support the existence of an Archean lithospheric mantle beneath this part of the NCC during the Middle Ordovician (Gao et al., 2002; Wu et al., 2006; Zhang et al., 2008; Chu et al., 2009).

The NCC was magmatically and tectonically quiescent from the Mesoproterozoic to the Early Paleozoic. This quiet period ended in the middle Ordovician with the eruption of the Mengyin and Fuxian kimberlites (Dobbs et al., 1994; Lu and Zheng, 1996; Yang et al., 2009a). Since the Late Mesozoic, intensive deformation, mineralization and igneous activity were widespread in the eastern NCC, and this resurgence in activity has been related to the removal of the cratonic mantle (Yang et al., 2003; Wu et al., 2005).

2.2. Sample description

Both Neogene basalts and Cretaceous–Eocene barren carbonatitic kimberlites outcrop at Hebi, which is located at the southern end of the TNCO (Fig. 1). The Neogene alkali basalts, which erupted ca 4 Ma ago (Liu et al., 1990), contain abundant mantle xenoliths and megacrysts of garnet and pyroxene (Zheng et al., 2001, 2007). The

Hebi mantle xenoliths are quite fresh and usually have rounded shapes, with diameters of 2–3 cm. They are mainly spinel harzburgites with a modal content of clinopyroxene less than 5%. Although phlogopite has been reported in the Hebi mantle xenoliths (Zhao et al., 2007), it has not been observed in any samples selected in the present study. The Hebi mantle xenoliths commonly display coarse-grained microstructures, in which the grain sizes of olivine and orthopyroxene are generally from 2 to 10 mm. Triple-junction textures are widely developed among the silicate minerals and kink-banding is commonly observed in olivine. A few samples show porphyroclastic microstructures, in which olivine occurs as coarse and commonly strained porphyroclasts set in a matrix of small strain-free recrystallized grains. Small rounded grains of spinel are interstitial between olivine and orthopyroxene. Shear deformation has not been observed in any Hebi mantle xenoliths. Alkali- and aluminum-rich glass occurs as small veins in some samples.

3. Analytical methods

3.1. Whole rock and mineral major elements

Whole-rock major elements of HB01, HB07, HB08 and HB13 were measured by XRF at Northwest University in Xi'an, whereas other samples were analysed at the Institute of Geology and Geophysics, Chinese Academy of Sciences (IGGCAS). The method used at Northwest University has been described by Rudnick et al. (2004). The analytical uncertainty ranges from 1% to 3%. Major-element compositions of minerals were analysed on a JEOL JXA-8100 Electron Probe at IGGCAS, using a 15 keV accelerating voltage and a 10 nA beam current.

3.2. Clinopyroxene trace elements

Trace elements in clinopyroxene were analysed using a laser ablation inductively coupled plasma mass spectrometer (LA-ICP-MS) at IGGCAS. The detailed description of the method has been given by Liu et al. (2010a). The LA-ICP-MS system consists of a Lambda Physik LPX 120I pulsed ArF excimer laser coupled to an Agilent 7500 ICP-MS. Isotopes were measured in peak-hopping mode. A spot size of 80 μm and repetition rate of 8 Hz were used. The NIST612 glass was used as an external calibration standard and the

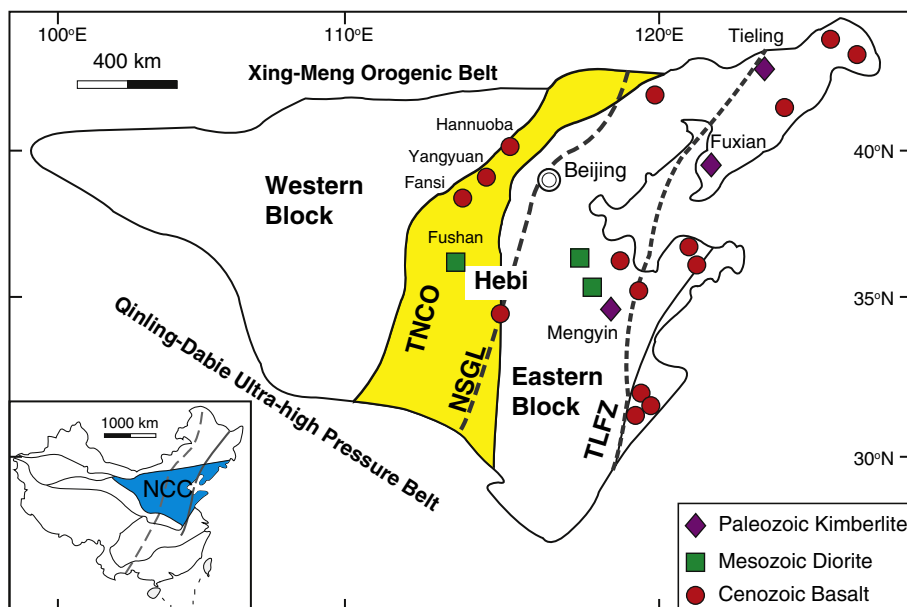


Fig. 1. Sketch map showing the distribution of mantle xenoliths trapped by the Paleozoic kimberlites, the Mesozoic diorites and the Cenozoic basalts in North China Craton (NCC). The tectonic subdivisions of the NCC are from (Zhao et al., 2001). TNCO: Trans-North China Orogen; NSGL: North-South Gravity Lineament; TLFZ: Tan-Lu Fault Zone.

Table 1Whole-rock major-element compositions of the Hebi mantle xenoliths. Total iron is expressed as Fe₂O₃.

Sample	HB01	HB07	HB08	HB13	HB20	HB21	HB22	HB23	HB32	HB32-R	HB33	HB34	HB38	HB39
SiO ₂	43.08	42.30	43.48	43.31	43.92	45.95	43.98	42.03	43.33	43.26	44.65	46.60	43.04	44.29
TiO ₂	0.04	0.01	0.08	0.02	0.03	0.03	0.03	0.02	0.06	0.06	0.03	0.04	0.02	0.01
Al ₂ O ₃	1.42	0.57	2.56	1.05	1.02	1.69	1.09	1.05	1.44	1.44	0.80	1.65	0.33	0.91
Fe ₂ O ₃	7.52	7.78	7.88	7.90	8.13	7.59	8.96	7.67	9.02	9.08	8.14	7.07	8.53	7.88
MnO	0.09	0.09	0.10	0.10	0.11	0.11	0.11	0.10	0.12	0.12	0.11	0.10	0.11	0.11
MgO	44.98	47.91	42.60	45.56	45.36	42.67	44.75	44.71	44.31	44.39	44.91	42.71	47.28	45.29
CaO	0.94	0.25	0.74	0.51	0.58	0.88	0.45	0.34	0.44	0.44	0.60	0.61	0.23	0.59
Na ₂ O	<0.01	<0.01	0.02	<0.01	0.00	0.11	0.01	0.09	0.02	0.02	0.05	0.10	0.00	0.02
K ₂ O	0.17	0.07	0.51	0.06	0.08	0.23	0.09	0.17	0.05	0.05	0.07	0.14	0.04	0.06
P ₂ O ₅	0.03	0.02	0.06	0.03	0.04	0.02	0.02	0.02	0.02	0.02	0.01	0.02	0.01	0.11
LOI	0.79	0.04	1.10	0.55	0.08	0.04	0.16	0.14	0.42	0.44	0.06	0.28	0.28	0.02
Total	99.06	99.04	99.13	99.09	99.36	99.32	99.33	96.97	99.84	99.93	99.79	99.88	99.71	99.84
Mg#	0.92	0.92	0.92	0.92	0.92	0.92	0.91	0.92	0.91	0.91	0.92	0.92	0.92	0.92

R: replicate analysis

All Fe is expressed as Fe₂O₃

LOI: loss on ignition

Mg#: molar Mg/(Mg + Fe)

isotope ⁴³Ca was used as an internal standard. The analytical uncertainty of the LA-ICPMS method is ca 5–10%.

3.3. Bulk-rock Re–Os isotopes

Bulk-rock Re–Os isotopes were analysed by isotope dilution at IGGCAS, following the procedure described by Chu et al., (2009). About 1–1.5 g powder, together with Re–Os isotope spikes (i.e., ¹⁸⁷Re and ¹⁹⁰Os) and reverse aqua regia (3 ml 12 N HCl and 6 ml 16 N HNO₃), was digested in a Carius Tube at 240 °C for 48–72 h. Osmium was extracted from the aqua regia solution by solvent extraction into CCl₄ and further purified by micro-distillation. Rhenium was separated from the solution by anion exchange chromatography using a 2 ml resin (AG-1×8, 100–200 meshes). Osmium isotopes were measured by N-TIMS on a GV Isoprobe-T instrument in a static mode using Faraday Cup. To increase the ionization efficiency, Ba(OH)₂ solution was used as an ion emitter. The measured Os isotopic ratios were corrected for mass fractionation assuming ¹⁹²Os/¹⁸⁸Os = 3.0827. The in-run precision for Os isotopic measurements was better than 0.2% (2σ; σ = relative standard deviation) for most samples, but higher for samples HB-22 and HB-44. The Johnson-Matthey standard of UMD was used as an external standard and its ratio was 0.11378 ± 2 during the measurements of samples for this paper. Rhenium isotopes were measured on a Thermal-Electron Neptune MC-ICPMS using an electron multiplier in a peak-jumping mode or Faraday cups in a static mode, depending on the measured signal intensity. The total procedural blank is 3 pg for Re and 2–3 pg for Os.

3.4. In-situ clinopyroxene Sr isotopes

The Sr-isotope compositions of clinopyroxenes were measured in thin sections by laser ablation, with the cell coupled to a Neptune multi-collector ICP-MS. Detailed descriptions of the instrument and the laser ablation system have been given in previous studies (Yang et al., 2009a,b). The MC-ICPMS instrument is equipped with eight motorized Faraday cups and one fixed central channel, where the ion beam can be switched between a Faraday cup and a SEM detector. Isotopes were acquired in a static multi-collector mode with low resolution using nine Faraday collectors and the mass configuration array from ⁸³Kr to ⁸⁸Sr, applying the technique of Ramos et al. (2004). Prior to analysis, collectors were aligned using a tuning solution containing Rb, Sr, Er and Yb. The operation parameters were further optimized by an aliquot of 200 ppb NIST SRM987 solution to get maximum intensity. A laser pulse energy of ~120 mJ, repetition rate of 10 Hz and spot size of 160 μm were used during the analyses.

Several relevant interferences were monitored during laser ablation analysis. As in the method employed by Ramos et al. (2004), a 50-second measurement of the gas blank was taken prior to ablation in order to correct for Kr interference during each analysis. The natural Kr ratios of ⁸³Kr/⁸⁴Kr = 0.20175 and ⁸³Kr/⁸⁶Kr = 0.66474 were used for interference correction. The natural ⁸⁵Rb/⁸⁷Rb ratio of 2.5926 was used to correct the interference of ⁸⁷Rb on ⁸⁷Sr. Samples with Rb/Sr ratios less than 0.02 (⁸⁵Rb/⁸⁷Sr < 0.06) can be effectively corrected by this method (Yang et al., 2009a). The interferences of doubly-charged rare earth elements (REE) have been corrected by monitoring the peaks of ¹⁶⁷Er²⁺, ¹⁷¹Yb²⁺, and ¹⁷³Yb²⁺ at masses of 83.5, 85.5 and 86.5, using the method of Ramos et al. (2004). However, no correction for ¹⁷⁶Lu²⁺ or ¹⁷⁶Hf²⁺ on ⁸⁸Sr was made since their intensities are low in our analyses. The effectiveness of the interference corrections can

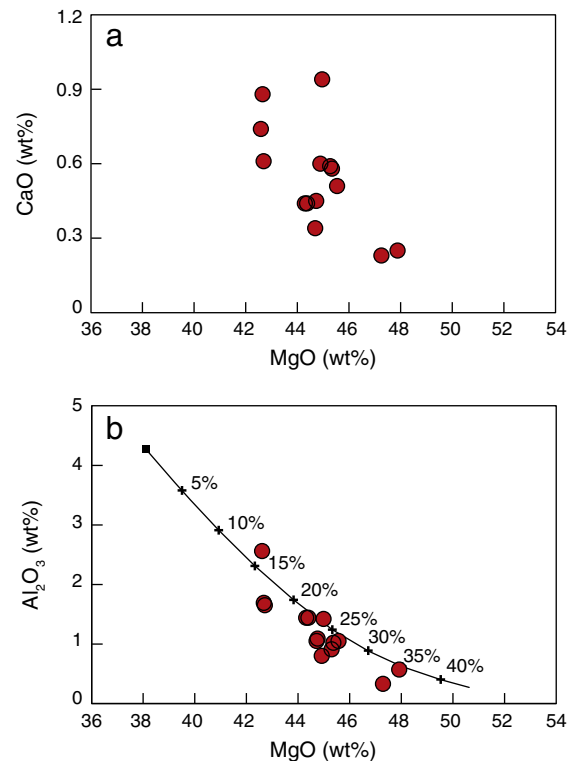


Fig. 2. Whole-rock MgO vs. CaO (a) and Al₂O₃ (b). The curve represents the residue compositions formed by equilibrium melting of fertile peridotite KR-4003 at 2 GPa (Herzberg, 2004).

Table 2
Major-element compositions of minerals in the Hebi mantle xenoliths. Total iron is expressed as FeO. $Mg^{\#} = Mg/(Mg + Fe)$ and $Cr^{\#} = Cr/(Cr + Al)$. Degrees of partial melting (F) have been calculated from the spinel $Cr^{\#}$ using $F = 10 * Ln(Cr^{\#}) + 24$ (Hellebrand et al., 2001).

	HB01				HB02				HB07				HB09				HB10			
	Ol	Sp	Opx	Cpx	Ol	Sp	Opx	Cpx	Ol	Sp	Opx	Cpx	Ol	Sp	Opx	Cpx	Ol	Sp	Opx	Cpx
SiO ₂	41.36	0.06	56.20	53.35	41.45	0.10	55.26	53.65	41.03	0.07	56.05	53.56	41.41	0.10	56.35	52.11	40.81	0.03	54.98	52.05
TiO ₂	0.04	0.11	0.03	0.09	0.03	0.07	0.08	0.03	0.04	0.04	0.07	0.05	0.08	0.06	0.03	1.90	0.00	0.11	0.04	0.27
Al ₂ O ₃	0.01	26.47	2.77	3.50	0.01	33.95	3.37	3.85	0.00	31.00	3.09	4.11	0.01	32.90	3.27	1.94	0.01	42.38	3.82	5.20
Cr ₂ O ₃	0.04	42.44	0.77	1.61	0.06	35.26	0.80	1.28	0.04	38.41	0.78	1.63	0.03	36.58	0.84	0.71	0.02	23.77	0.66	1.23
FeO	7.39	13.87	4.57	2.28	8.25	12.97	5.01	2.66	7.48	13.30	4.71	2.36	7.80	13.63	4.79	3.48	7.64	12.31	4.95	2.73
MnO	0.08	0.19	0.12	0.14	0.11	0.15	0.12	0.12	0.19	0.13	0.11	0.08	0.12	0.14	0.09	0.10	0.12	0.15	0.11	0.09
MgO	50.37	16.81	34.13	17.00	50.08	17.48	33.01	16.98	50.93	17.60	33.73	16.15	50.15	17.44	33.72	16.04	49.92	19.66	32.90	15.46
CaO	0.06	0.02	0.99	20.96	0.06	0.02	0.96	19.06	0.07	0.04	0.89	19.47	0.09	0.01	1.00	23.17	0.07	0.01	0.92	20.59
NiO	0.45	0.19	0.10	0.10	0.45	0.24	0.10	0.05	0.41	0.25	0.09	0.05	0.39	0.26	0.14	0.10	0.38	0.29	0.11	0.04
Na ₂ O	0.04	0.02	0.09	1.17	0.02	0.02	0.20	1.78	0.02	0.02	0.14	1.62	0.04	0.01	0.12	0.69	0.01	0.00	0.15	1.58
K ₂ O	0.02	0.02	0.04	0.05	0.02	0.00	0.00	0.03	0.03	0.03	0.00	0.00	0.39	0.02	0.03	0.06	0.01	0.00	0.00	0.01
Total	99.84	100.17	99.81	100.25	100.54	100.27	98.93	99.47	100.23	100.86	99.67	99.09	100.09	101.09	100.37	100.28	98.98	98.71	98.64	99.25
Mg [#]	92.5	0.69	0.93	0.93	91.6	0.71	0.92	0.92	92.5	0.70	0.93	0.92	92.1	0.70	0.93	0.89	92.1	0.74	0.92	0.91
Cr [#]		0.52				0.41				0.45				0.43				0.28		
F (%)		17				15				16				15				11		
	HB13				HB18				HB20				HB21				HB22			
	Ol	Sp	Opx	Cpx	Ol	Sp	Opx	Cpx	Ol	Sp	Opx	Cpx	Ol	Sp	Opx	Cpx	Ol	Sp	Opx	Cpx
SiO ₂	41.07	0.00	56.29		41.53	0.01	56.04	53.11	40.94	0.03	56.15	53.63	40.58		54.87	52.34	41.12		55.99	53.26
TiO ₂	0.00	0.02	0.01		0.00	0.05	0.08	0.01	0.01	0.01	0.01	0.01	0.01		0.01	0.01	0.02		0.01	0.02
Al ₂ O ₃	0.01	29.49	2.82		0.00	30.06	2.51	3.72	0.02	26.59	2.67	2.80	0.02		3.43	3.61	0.02		2.74	4.31
Cr ₂ O ₃	0.03	38.40	0.73		0.01	36.09	0.65	1.46	0.04	43.13	0.79	1.23	0.03		0.85	1.25	0.05		0.83	2.15
FeO	7.61	13.27	4.85		7.60	15.93	5.57	2.70	8.06	14.28	5.08	2.40	8.28		5.28	2.52	8.62		5.43	2.72
MnO	0.10	0.20	0.13		0.11	0.26	0.14	0.10	0.12	0.13	0.12	0.07	0.11		0.12	0.08	0.10		0.11	0.08
MgO	50.60	16.73	33.87		50.58	16.66	33.43	16.47	50.59	16.39	34.04	17.50	49.79		33.27	17.17	49.58		33.21	15.84
CaO	0.09	0.00	1.04		0.03	0.01	0.87	20.43	0.08	0.00	1.01	21.28	0.08		1.04	21.68	0.07		0.96	18.71
NiO	0.40	0.19	0.10		0.38	0.22	0.01	0.06	0.37	0.18	0.12	0.06	0.39		0.10	0.08	0.36		0.10	0.07
Na ₂ O	0.00	0.00	0.05		0.01	0.03	0.10	1.41	0.01	0.01	0.10	1.00	0.01		0.09	0.70	0.02		0.20	2.09
K ₂ O	0.00	0.00	0.01		0.01	0.00	0.09	0.00	0.01	0.00	0.01	0.01	0.01		0.01	0.01	0.01		0.01	0.01
Total	99.91	98.31	99.89		100.24	99.30	99.49	99.48	100.24	100.75	100.10	99.98	99.32		99.09	99.45	99.97		99.59	99.25
Fo	92.2	0.69	0.93		92.2	0.65	0.91	0.92	91.8	0.67	0.92	0.93	91.5		0.92	0.92	91.1		0.92	0.91
Cr [#]		0.47				0.45				0.52										
F (%)		16				16				17										
	HB23				HB25				HB28				HB32				HB33			
	Ol	Sp	Opx	Cpx	Ol	Sp	Opx	Cpx	Ol	Sp	Opx	Cpx	Ol	Sp	Opx	Cpx	Ol	Sp	Opx	Cpx
SiO ₂	40.92	0.05	55.71		40.03	0.05	54.99	52.39	40.58	0.05	55.74	53.01	40.76	0.04	54.84	50.61	40.50	0.08	55.51	52.81
TiO ₂	0.01	0.02	0.01		0.01	0.02	0.03	0.01	0.01	0.05	0.01	0.01	0.01	0.50	0.07	1.03	0.02	0.23	0.04	0.19
Al ₂ O ₃	0.01	28.85	2.88		0.01	32.70	3.23	3.32	0.02	26.88	2.67	2.74	0.03	48.48	3.24	7.59	0.02	33.17	3.00	3.48
Cr ₂ O ₃	0.02	40.55	0.80		0.03	35.81	0.84	1.17	0.03	42.03	0.80	1.22	0.02	17.83	0.77	1.10	0.04	35.35	0.75	1.26
FeO	7.88	13.58	4.98		8.44	13.93	5.40	2.59	8.03	14.40	5.16	2.31	9.29	12.56	5.97	3.24	8.55	13.70	5.34	2.67
MnO	0.10	0.12	0.10		0.12	0.12	0.11	0.06	0.11	0.14	0.12	0.07	0.12	0.09	0.12	0.09	0.12	0.11	0.13	0.08
MgO	50.61	16.43	33.77		50.08	16.95	33.78	17.31	50.54	15.98	34.10	17.47	49.70	19.57	32.75	15.08	49.74	17.41	33.08	17.25
CaO	0.09	0.01	1.04		0.09	0.01	1.07	21.18	0.08	0.01	1.04	21.60	0.07	0.00	1.00	18.03	0.09	0.01	1.05	20.37
NiO	0.39	0.20	0.09		0.40	0.22	0.10	0.06	0.35	0.20	0.11	0.06	0.39	0.32	0.06	0.05	0.36	0.19	0.10	0.04
Na ₂ O	0.01	0.02	0.03		0.01	0.01	0.07	0.94	0.01	0.01	0.10	0.96	0.02	0.02	0.22	2.50	0.02	0.00	0.13	1.34
K ₂ O	0.01	0.00	0.00		0.01	0.01	0.01	0.01	0.01	0.00	0.01	0.01	0.01	0.00	0.01	0.02	0.00	0.00	0.00	0.01
Total	100.07	99.84	99.43		99.23	99.81	99.62	99.04	99.78	99.75	99.86	99.46	100.44	99.41	99.04	99.35	99.45	100.24	99.12	99.50
Fo	92.0	0.68	0.92		91.4	0.68	0.92	0.92	91.8	0.66	0.92	0.93	90.5	0.74	0.91	0.89	91.2	0.69	0.92	0.92
Cr [#]		0.49				0.42				0.51				0.20				0.42		
F (%)		17				15				17				8				15		

	HB34			HB35				HB36			HB38			HB39			
	Ol	Sp	Opx	Ol	Sp	Opx	Cpx	Ol	Opx	Cpx	Ol	Sp	Opx	Ol	Sp	Opx	Cpx
SiO ₂	40.83	0.03	55.70	41.23	0.03	55.48	52.52	40.95	55.96	52.52	40.79	0.06	56.24	40.84	0.05	55.84	52.74
TiO ₂	0.02	0.03	0.03	0.02	0.01	0.01	0.02	0.02	0.02	0.01	0.03	0.01	0.02	0.01	0.08	0.01	0.06
Al ₂ O ₃	0.02	31.43	3.17	0.01	37.31	3.31	3.22	0.02	3.10	4.10	0.02	29.23	2.90	0.02	28.89	2.80	3.35
Cr ₂ O ₃	0.03	37.41	0.83	0.02	30.56	0.62	0.83	0.04	0.86	1.77	0.04	40.13	0.85	0.04	39.68	0.78	1.43
FeO	7.50	13.58	4.87	7.74	13.60	4.98	2.22	7.92	4.97	2.43	8.03	13.14	5.08	8.03	13.96	5.13	2.51
MnO	0.10	0.11	0.11	0.10	0.11	0.11	0.07	0.11	0.11	0.07	0.10	0.11	0.12	0.12	0.13	0.12	0.08
MgO	50.21	17.44	33.64	50.12	17.87	33.69	16.98	49.89	33.54	16.55	49.28	16.34	33.37	49.57	16.23	33.44	17.05
CaO	0.08	0.01	0.93	0.06	0.01	0.75	22.59	0.08	1.02	20.10	0.08	0.01	1.03	0.08	0.01	1.00	20.78
NiO	0.39	0.19	0.09	0.40	0.24	0.11	0.05	0.33	0.09	0.05	0.40	0.18	0.11	0.36	0.20	0.12	0.05
Na ₂ O	0.01	0.01	0.15	0.01	0.01	0.04	0.54	0.02	0.08	1.42	0.01	0.02	0.04	0.03	0.01	0.09	1.16
K ₂ O	0.01	0.01	0.01	0.01	0.01	0.01	0.01	0.01	0.01	0.01	0.01	0.01	0.01	0.01	0.01	0.01	0.02
Total	99.19	100.24	99.51	99.74	99.78	99.10	99.06	99.38	99.76	99.03	98.78	99.25	99.77	99.11	99.25	99.35	99.22
Fo	92.3	0.70	0.92	92.0	0.70	0.92	0.93	91.8	0.92	0.92	91.6	0.69	0.92	91.7	0.67	0.92	0.92
Cr#		0.44			0.35							0.48			0.48		
F (%)		16			14							17			17		

	HB43				HB44				HB45				HB47				HB48			
	Ol	Sp	Opx	Cpx	Ol	Sp	Opx	Cpx	Ol	Sp	Opx	Cpx	Ol	Sp	Opx	Cpx	Ol	Sp	Opx	Cpx
SiO ₂	40.49	0.04	56.05	53.13	40.52	0.06	55.94	52.87	40.95	0.11	56.34	53.23	41.04	0.07	55.73	52.88	40.95	0.04	56.34	53.07
TiO ₂	0.02	0.32	0.01	0.21	0.01	0.13	0.04	0.06	0.01	0.03	0.01	0.03	0.01	0.09	0.02	0.06	0.01	0.07	0.02	0.04
Al ₂ O ₃	0.02	21.92	2.21	4.20	0.02	27.67	2.75	3.43	0.02	29.84	2.95	3.00	0.02	33.51	3.25	3.80	0.02	28.08	2.68	2.77
Cr ₂ O ₃	0.05	46.60	0.72	1.89	0.03	39.95	0.75	1.50	0.04	39.54	0.86	1.21	0.04	35.61	0.82	1.21	0.05	42.14	0.81	1.22
FeO	8.55	15.39	5.22	2.75	8.05	15.22	5.17	2.54	7.91	13.09	4.99	2.31	8.17	13.38	5.14	2.56	7.94	12.71	4.97	2.26
MnO	0.11	0.12	0.10	0.07	0.11	0.13	0.11	0.07	0.11	0.11	0.12	0.07	0.10	0.11	0.12	0.08	0.12	0.10	0.12	0.08
MgO	49.81	15.38	33.90	16.19	49.68	16.28	33.72	16.90	49.83	16.88	33.48	17.52	49.88	17.30	33.02	17.13	49.36	16.26	33.46	17.34
CaO	0.07	0.01	0.93	18.48	0.08	0.01	0.91	21.11	0.09	0.01	1.01	21.81	0.09	0.01	1.04	21.17	0.08	0.01	1.03	21.60
NiO	0.41	0.15	0.12	0.05	0.39	0.19	0.12	0.08	0.38	0.16	0.12	0.06	0.40	0.21	0.08	0.06	0.43	0.19	0.12	0.08
Na ₂ O	0.01	0.01	0.20	2.47	0.01	0.01	0.08	1.10	0.00	0.02	0.03	0.49	0.01	0.00	0.06	0.71	0.01	0.01	0.05	0.55
K ₂ O	0.01	0.00	0.01	0.00	0.01	0.01	0.01	0.01	0.02	0.01	0.01	0.02	0.00	0.01	0.01	0.01	0.01	0.01	0.01	0.01
Total	99.54	99.94	99.48	99.43	98.92	99.67	99.60	99.68	99.35	99.80	99.91	99.75	99.75	100.30	99.28	99.67	98.98	99.62	99.61	99.01
Fo	91.2	0.64	0.92	0.91	91.7	0.66	0.92	0.93	91.8	0.70	0.92	0.93	91.6	0.70	0.92	0.92	91.7	0.70	0.92	0.93
Cr#		0.59				0.49				0.47				0.42				0.50		
F (%)		19				17				16				15				17		

	HB49			HB50				HB54				HB57				HB62			
	Ol	Opx	Cpx	Ol	Sp	Opx	Cpx	Ol	Sp	Opx	Cpx	Ol	Sp	Opx	Cpx	Ol	Sp	Opx	Cpx
SiO ₂	41.08	55.71	51.69	40.75	0.04	55.82	53.98	40.90	0.05	55.53	53.27	41.28	0.03	55.58	52.41	40.70	0.10	56.18	52.79
TiO ₂	0.02	0.05	0.57	0.02	0.11	0.03	0.05	0.01	0.04	0.01	0.03	0.02	0.15	0.02	0.08	0.02	0.24	0.06	0.15
Al ₂ O ₃	0.02	3.55	3.09	0.01	27.73	2.67	3.35	0.03	33.22	3.21	3.73	0.02	28.89	2.86	3.54	0.02	27.69	2.63	4.47
Cr ₂ O ₃	0.02	0.61	1.55	0.04	41.53	0.80	1.27	0.02	36.03	0.81	1.30	0.03	39.64	0.72	1.44	0.02	39.51	0.72	1.74
FeO	8.28	5.30	2.64	8.08	14.04	5.08	2.57	7.85	12.90	4.97	2.41	8.09	14.62	5.19	2.51	8.08	15.69	5.16	2.72
MnO	0.11	0.11	0.10	0.11	0.13	0.11	0.08	0.10	0.10	0.11	0.06	0.11	0.14	0.12	0.08	0.11	0.13	0.11	0.07
MgO	50.30	33.18	16.06	49.54	16.17	33.21	17.04	49.97	17.21	33.05	16.75	50.06	16.41	33.53	16.90	49.98	16.25	33.67	16.07
CaO	0.06	0.92	22.90	0.07	0.01	0.95	19.75	0.08	0.01	0.99	20.50	0.07	0.01	0.92	21.21	0.07	0.01	0.95	19.81
NiO	0.41	0.09	0.06	0.37	0.19	0.11	0.05	0.37	0.22	0.12	0.06	0.39	0.23	0.11	0.04	0.39	0.22	0.12	0.06
Na ₂ O	0.01	0.21	0.65	0.01	0.02	0.16	1.55	0.01	0.01	0.12	1.33	0.01	0.01	0.08	1.00	0.01	0.01	0.12	1.74
K ₂ O	0.01	0.01	0.02	0.01	0.00	0.01	0.00	0.01	0.01	0.00	0.02	0.01	0.00	0.01	0.01	0.01	0.01	0.01	0.05
Total	100.31	99.74	99.32	99.02	99.97	98.95	99.69	99.35	99.80	98.92	99.47	100.09	100.13	99.14	99.23	99.42	99.85	99.72	99.66
Fo	91.5	0.92	0.92	91.6	0.67	0.92	0.92	91.9	0.70	0.92	0.93	91.7	0.67	0.92	0.92	91.7	0.65	0.92	0.91
Cr#					0.50				0.42				0.48				0.49		
F (%)					17				15				17				17		

Table 3
Trace-element compositions of clinopyroxenes in Hebi mantle xenoliths. n: chondrite-normalized (Anders and Grevesse, 1989).

	HB01	HB02	HB05	HB07	HB09	HB10	HB18	HB20	HB21	HB22	HB25	HB32	HB33	HB35	HB36	HB39	HB43	HB44	HB50	HB54	HB62
Sc	51.0	76.5	33.2	65.2	80.8	73.9	80.8	65.8	53.2	82.5	50.8	47	54	62	71	69	85	70	63	72	78
Ti	342	327	13173	192	116	1593	177	341	48	228	18	6999	1892	102	165	788	840	448	351	945	1136
V	98	218	459	125	204	230	178	187	170	251	206	233	126	123	181	211	227	178	177	177	249
Cr	11278	10235	21	9231	11629	9517	9824	9432	8592	16192	8126	7883	10424	5595	11522	9881	14791	10877	7302	9966	12128
Sr	389	206	194	478	403	595	474	449	242	298	130	250	227	516	407	519	402	592	481	347	947
Y	2.04	5.01	13.14	3.33	3.06	9.51	4.67	2.30	0.713	4.89	0.386	15.40	3.80	0.79	5.35	3.43	11.53	2.14	3.89	3.62	3.84
Zr	31.4	19.2	116.7	36.7	26.3	34.2	16.6	26.2	0.6	74.7	0.13	183.7	38.7	10.0	70.2	71.7	106.0	22.1	35.7	37.0	38.8
Nb	0.44	0.86	1.31	1.50	2.57	2.14	0.71	2.57	0.67	4.07	1.65	4.43	11.07	6.34	2.13	4.78	8.26	2.11	2.90	3.72	1.95
Ba	0.20	0.39	0.16	1.79	1.01	4.25	0.20	14.30	0.31	63.49	0.41	12.80	241	86.0	1.42	34.0	18.6	67.5	12.5	9.88	11.29
La	4.35	5.61	3.95	7.35	14.36	4.74	7.04	10.16	4.41	10.78	6.97	10.33	6.95	3.50	11.01	21.00	6.09	14.95	17.82	13.38	9.71
Ce	16.23	18.07	16.13	28.89	41.55	20.36	32.34	34.22	9.16	28.70	12.38	31.65	17.64	8.89	32.87	49.73	24.27	38.54	48.94	37.51	42.70
Pr	2.87	2.79	2.87	4.62	5.77	3.62	6.08	4.75	0.93	4.00	1.08	4.51	2.25	0.97	4.62	5.63	4.37	4.90	6.09	5.03	7.96
Nd	16.98	13.84	16.55	22.68	25.14	18.99	29.32	20.26	3.41	18.34	3.38	22.55	9.91	3.39	21.60	22.42	24.40	19.62	25.63	22.13	40.08
Sm	4.65	3.24	5.29	4.82	4.09	4.37	4.86	3.33	0.50	3.94	0.365	6.07	2.07	0.36	4.66	3.58	6.51	3.15	4.87	3.66	6.87
Eu	1.22	1.05	1.89	1.38	1.11	1.29	1.21	0.91	0.13	1.28	0.094	2.01	0.68	0.08	1.35	1.02	2.07	0.84	1.43	1.05	1.66
Gd	2.42	2.70	5.06	3.07	2.87	3.39	2.62	2.10	0.51	2.87	0.366	5.81	1.78	0.30	3.61	2.39	5.57	2.06	3.28	2.52	3.61
Tb	0.20	0.29	0.73	0.27	0.25	0.42	0.25	0.17	0.03	0.32	0.02	0.78	0.20	0.03	0.37	0.23	0.66	0.17	0.33	0.26	0.30
Dy	0.72	1.37	3.95	1.12	0.98	2.30	1.12	0.72	0.15	1.46	0.06	4.01	1.02	0.12	1.61	1.08	3.23	0.65	1.29	1.11	1.23
Ho	0.08	0.19	0.60	0.14	0.13	0.38	0.18	0.10	0.03	0.20	0.02	0.64	0.16	0.03	0.23	0.15	0.46	0.09	0.16	0.15	0.15
Er	0.14	0.39	1.30	0.26	0.22	0.94	0.42	0.19	0.11	0.58	0.10	1.38	0.36	0.16	0.35	0.31	0.89	0.19	0.26	0.32	0.35
Tm	0.02	0.05	0.13	0.03	0.03	0.12	0.06	0.03	0.03	0.08	0.02	0.15	0.05	0.04	0.04	0.04	0.08	0.03	0.03	0.04	0.04
Yb	0.10	0.34	0.56	0.22	0.23	0.82	0.40	0.19	0.20	0.52	0.21	0.88	0.32	0.29	0.26	0.28	0.48	0.20	0.22	0.24	0.25
Lu	0.02	0.06	0.07	0.03	0.05	0.12	0.07	0.03	0.04	0.08	0.03	0.11	0.04	0.05	0.04	0.04	0.05	0.03	0.04	0.05	0.03
Hf	0.84	0.56	5.49	0.91	0.42	0.97	0.34	0.55	0.03	1.51	0.02	5.73	0.96	0.17	0.58	2.30	2.33	0.59	0.60	0.83	1.76
Ta	0.05	0.18	0.33	0.21	0.22	0.09	0.07	0.30	0.05	0.22	0.17	0.48	0.31	0.10	0.40	0.53	0.63	0.13	0.25	0.24	0.15
Th	0.17	0.24	0.07	0.30	0.80	0.24	0.16	0.35	0.34	0.53	0.65	0.70	0.47	0.17	0.46	1.32	0.16	0.73	0.83	0.69	0.39
U	0.05	0.07	0.02	0.09	0.25	0.07	0.05	0.13	0.13	0.07	0.15	0.28	0.17	0.98	0.41	0.47	0.08	0.27	0.31	0.24	0.16
(La/Yb) _n	29.3	11.4	4.9	23.6	44.1	4.0	12.1	37.1	15.1	14.5	22.8	8.1	15.3	8.3	29.8	51.1	8.7	52.7	55.3	38.9	27.2

be evaluated by comparing the measured $^{84}\text{Sr}/^{86}\text{Sr}$ and $^{84}\text{Sr}/^{88}\text{Sr}$ ratios to their accepted values (0.0565 and 0.00675, respectively). Prior to sample analysis, both international (DUR) and in-house (SAP) apatite standards were used to evaluate the reliability of the laser ablation analyses, the calibration technique and matrix-matched effect. Twenty-two analyses of DUR and SAP yield average values of 0.70637 ± 11 (2SD) and 0.72645 ± 14 , respectively, which are identical to their values as measured by solution analysis (0.70629 ± 2 vs. 0.72655 ± 2 ; (McFarlane and McCulloch, 2008)) and laser methods (0.70638 ± 13 vs. 0.72652 ± 10 ; (Yang et al., 2009b)).

4. Results

4.1. Whole rock major elements

Whole-rock major-element compositions of Hebi mantle xenoliths are listed in Table 1. All samples are fresh with loss on ignition (LOI) values less than 1.1%. They have refractory compositions with high MgO contents (42.6–47.91%), but low CaO (0.23–0.94%), Al_2O_3 (0.33–2.56%), Na_2O (<0.11%) and TiO_2 (0.01–0.08%) contents. The bulk-rock Mg# [= molar $\text{Mg}/(\text{Mg} + \text{Fe})$] values vary from 0.91 to 0.92. The MgO contents show negative relationships with both CaO (Fig. 2a) and Al_2O_3 contents (Fig. 2b).

4.2. Mineral compositions

Major-element compositions of minerals are listed in Table 2, and trace-element data for clinopyroxenes are given in Table 3.

4.2.1. Olivine

Consistent with the classification by Zheng et al. (2001), the Hebi mantle xenoliths selected in the present study have been divided into two groups according to the Fo content of olivine [= $100 \times \text{Mg}/(\text{Mg} + \text{Fe})$], i.e., high-Fo group (Fo > 91) and low-Fo group (Fo < 91). All Hebi samples but HB32 with Fo contents of 91.1–92.5 belong to the high-Fo group, whereas sample HB32 has a lower olivine Fo of 90.5 (Fig. 3a). Olivines in the high-Fo samples have NiO contents of 0.33–0.45%, whereas olivine in low-Fo sample HB32 contains 0.39% NiO.

4.2.2. Spinel

The Cr# and Mg# of spinel in Hebi mantle xenoliths are negatively correlated (Fig. 3b). Spinel in the high-Fo samples have Cr# [= $\text{Cr}/(\text{Cr} + \text{Al})$] ranging from 0.28 to 0.59, whereas spinel in the low-Fo sample has a low Cr# of 0.2. The former has TiO_2 contents lower than the latter, i.e., 0.01–0.32% vs. 0.50%. Degrees of partial melting estimated from spinel Cr# (Hellebrand et al., 2001) are 11–19% for the high-Fo samples and 8% for the low-Fo sample (HB-32).

4.2.3. Orthopyroxene

Orthopyroxenes in the Hebi xenoliths have Mg# values of 0.91–0.93, and contain 0.75–1.07% CaO, 2.21–3.82% Al_2O_3 and 0.61–0.86% Cr_2O_3 . The Al_2O_3 contents show an inverse relationship with the Cr# of spinel in the high-Fo samples, whereas the low-Fo sample HB32 deviates from this correlation to low Al_2O_3 content (Fig. 4a). The ratios of Mg# between orthopyroxene and olivine approach unity, which suggests that equilibrium was attained in all the Hebi samples.

4.2.4. Clinopyroxene

Clinopyroxenes in all high-Fo samples but HB09 have Mg# ranging from 0.91–0.93 and contain 2.74–5.20% Al_2O_3 , 0.83–2.15% Cr_2O_3 , 0.49–2.47% Na_2O and 0.01–1.03% TiO_2 . Compared to other high-Fo samples, clinopyroxene in sample HB09 has low Mg# (0.89), Al_2O_3 (1.94%), Cr_2O_3 (0.70%) and Na_2O (0.69%), but high TiO_2 (1.90%). Clinopyroxene in the low-Fo sample HB32 has a lower Mg# (0.89), but higher Al_2O_3 (7.59%) and Na_2O (2.50%) than the high-Fo samples.

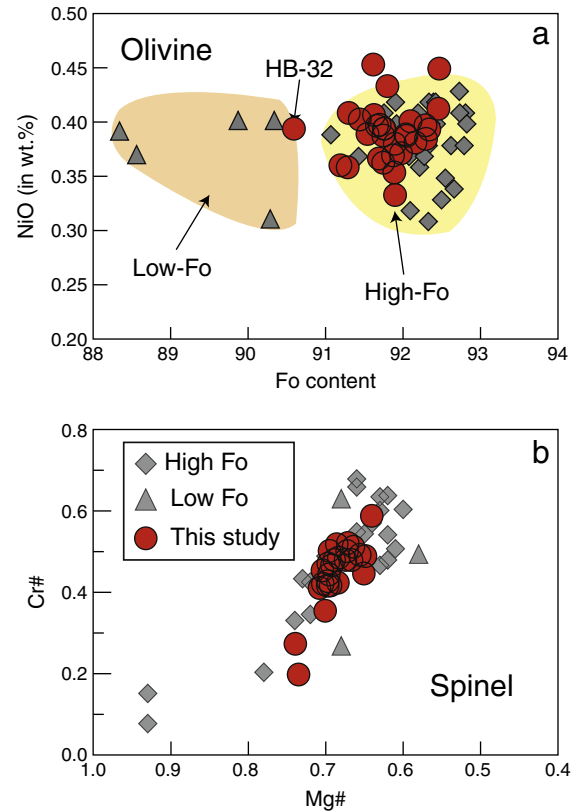


Fig. 3. Olivine Fo vs. NiO content (a) and spinel Cr# vs. Mg# (b). Compositions of the high-Fo and low-Fo mantle xenoliths reported by Zheng et al. (2001) are shown for comparison.

The MgO contents show negative correlations with Al_2O_3 , Na_2O and TiO_2 (Fig. 4b–d).

As in the previous study (Zheng et al., 2001), clinopyroxenes in Hebi mantle xenoliths display two different REE patterns. Clinopyroxenes in most xenoliths show sinusoidal REE patterns (Fig. 5a), i.e., with flat HREE, strong enrichment from Er to Nd but depleted LREE (La to Nd). In the trace-element diagram (Fig. 5b), they display enrichment in LILEs (e.g., Th and U) and negative anomalies in HFSEs (e.g., Zr, Hf, Nb, Ta and Ti). Clinopyroxenes in three samples (HB21, HB25 and HB35) display REE patterns with depletion from Lu to Dy and enrichment from Dy to La (Fig. 5c). Clinopyroxenes in both HB21 and HB25 also show marked negative anomalies in the HFSEs (Fig. 5d). Clinopyroxene in sample HB35 has a different trace-element pattern with weak negative anomalies in Nb, Ta, Zr and Hf.

4.3. Equilibrium temperatures

Mineral compositions indicate that equilibrium has been attained in the Hebi mantle xenoliths, thus enabling us to estimate the temperatures by using various geothermometers. Temperatures were calculated using two calibrations of the two-pyroxene geothermometer (Wells, 1977; Brey and Kohler, 1990), the Ca-in-orthopyroxene geothermometer (Brey and Kohler, 1990) and the Al-in-orthopyroxene geothermometer (Witt-Eickchen and Seck, 1991). The results are listed in Table 4 and plotted in Fig. 6. In general, there is a good agreement between the different methods, i.e., 905–1089 °C for two-pyroxene geothermometer of Brey and Kohler (1990), 985–1071 °C for Ca-in-orthopyroxene geothermometer of Brey and Kohler (1990), 813–1036 °C for Wells (1977) and 1009–1104 °C for Witt-Eickchen and Seck (1991). We have recalculated the temperatures of samples previously reported by Zheng et al. (2001), which give a range of 893–

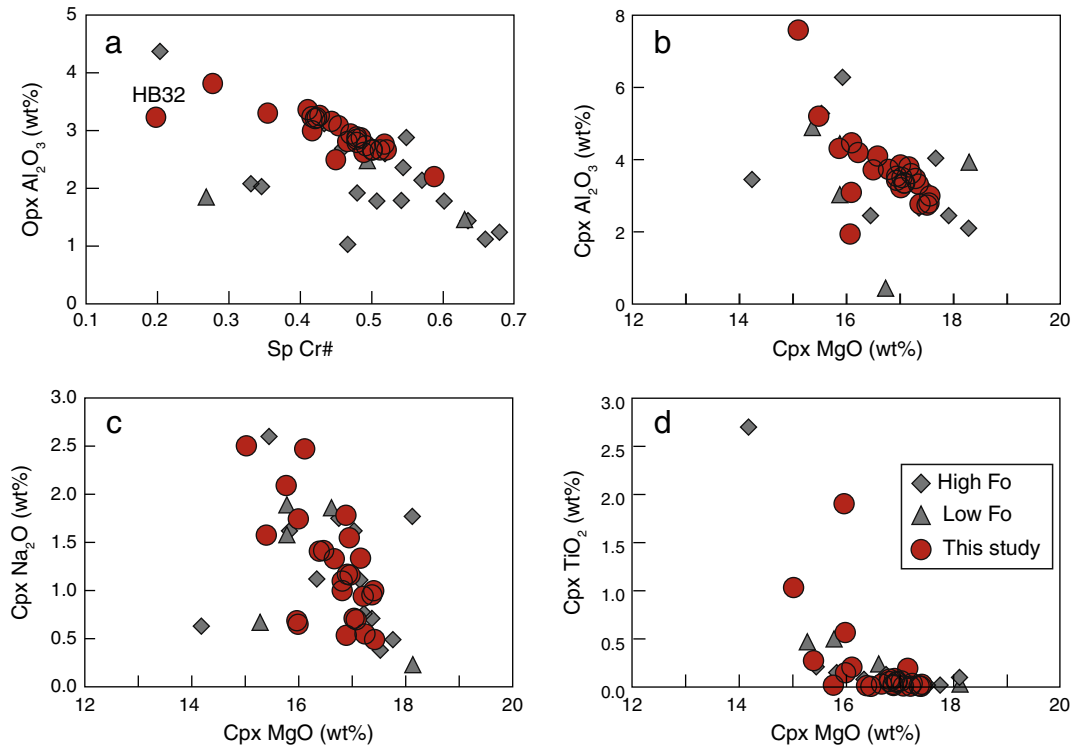


Fig. 4. Spinel Cr# vs. opx Al₂O₃ contents (a) and cpx MgO vs. Al₂O₃ (b), Na₂O (c) and TiO₂ (d). Symbols are same to the Fig. 3.

1177 °C. No garnet-bearing xenoliths have been found in Hebi, so we cannot construct a xenolith-based geotherm. However, the Hebi mantle xenoliths have similar high temperatures to the Cenozoic spinel-facies mantle xenoliths from the eastern NCC (Chu et al., 2009), implying a hot lithospheric geotherm beneath Hebi during the Cenozoic.

4.4. Re–Os isotopes

Bulk-rock Re–Os isotopes have been measured for eight samples and the results are given in Table 5. The Re contents range from 0.012 to 0.281 ppb. All the Hebi samples but HB44 have Os contents

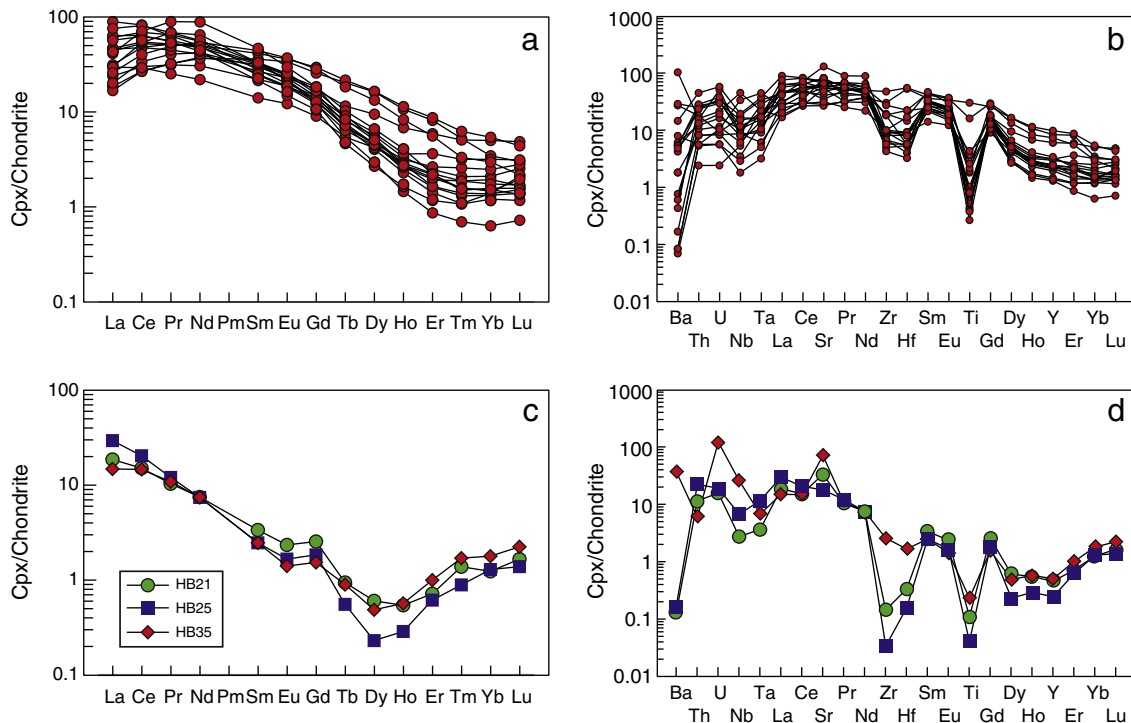


Fig. 5. Chondrite normalized REE patterns of clinopyroxenes in Hebi peridotites. Chondrite values are from (Anders and Grevesse, 1989).

Table 4
Equilibrium temperatures of Hebi mantle xenoliths calculated by various geothermometers. A pressure of 1.5 GPa is assumed for all calculations.

	Brey and Kohler (1990)	Brey and Kohler (1990)	Wells (1977)	Witt-Eickchen and Seck (1991)
	Ca-in-opx	Cpx-Opx	Cpx-Opx	Cr-Al in Opx
HB01	1050	1024	999	1043
HB07	1049	1090	1016	1062
HB09	1051		813	1088
HB10	1034	957	941	1054
HB13	1064			1026
HB-18	1020	1010	988	985
HB-20	1056	1015	1012	1047
HB-21	1066	1005	1011	1104
HB-22	1044	1075	1012	1073
HB-23	1065			1055
HB-25	1071	1021	1023	1087
HB-28	1064	978	993	1050
HB-32	1056	1089	1020	1074
HB-33	1067	1035	1030	1051
HB-34	1035			1084
HB-35	985	905	941	1009
HB-36	1059	1041	1015	1090
HB-38	1063			1075
HB-39	1055	1014	1009	1050
HB-43	1037	1062	1011	1011
HB-44	1031	997	992	1033
HB-45	1056	1027	1025	1080
HB-47	1066	1053	1036	1081
HB-48	1063	1023	1017	1054
HB-49	1033	1082	1005	1023
HB-50	1044	1072	1035	1057
HB-54	1053	1025	1007	
HB-57	1033	994	994	1029
HB-62	1042	1080	1018	1097

higher than 1 ppb (i.e., 1.33–5.69 ppb) and $^{187}\text{Re}/^{188}\text{Os}$ ratios varying from 0.03 to 0.74. Sample HB44 has the lowest contents of both Re and Os (0.012 ppb and 0.26 ppb, respectively), giving a $^{187}\text{Re}/^{188}\text{Os}$ ratio of 0.22. The Hebi mantle xenoliths have unradiogenic $^{187}\text{Os}/^{188}\text{Os}$ ratios of 0.11067–0.11688, which are similar to values reported in a recent study on Hebi mantle xenoliths (Liu et al., 2011b) but higher than those of two sulfide grains in Hebi mantle xenoliths analyzed previously (0.10651 and 0.11024; Zheng et al., 2007). Sample HB08 has the lowest $^{187}\text{Os}/^{188}\text{Os}$ ratio of 0.11067; this is the most unradiogenic bulk-rock ratio found in Cenozoic mantle xenoliths from the NCC (Gao et al., 2002; Wu et al., 2003, 2006; Xu et al., 2008; Chu et al., 2009; Zhang et al., 2009; Liu et al., 2010b). The Re

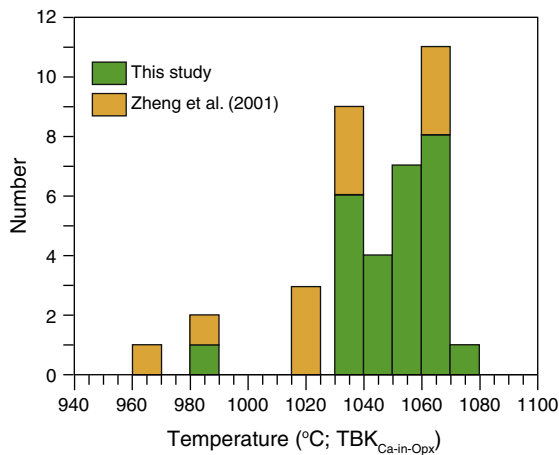


Fig. 6. Equilibrium temperature histogram of Hebi mantle xenoliths. Temperatures recalculated by mineral data reported by Zheng et al. (2001) are also shown for comparison.

Table 5
Whole-rock Re–Os isotope compositions of Hebi mantle xenoliths. T_{MA} : model ages; T_{RD} : Re depletion ages. Both T_{MA} and T_{RD} are calculated relative to the primitive upper mantle (PUM; (Meisel et al., 2001)) using the parameters: $\lambda = 1.666 \times 10^{11}$ /year, $(^{187}\text{Re}/^{188}\text{Os})_{PUM} = 0.423$, $(^{187}\text{Os}/^{188}\text{Os})_{PUM} = 0.1296$.

	Al ₂ O ₃	Re (ppb)	Os (ppb)	$^{187}\text{Re}/^{188}\text{Os}$	$^{187}\text{Os}/^{188}\text{Os}$	2 δ	T_{RD} (Ga)	T_{MA} (Ga)
HB02		0.034	5.69	0.029	0.11420	0.00011	2.1	2.3
HB08	2.56	0.033	3.43	0.047	0.11067	0.00010	2.6	2.9
HB13	1.05	0.063	2.09	0.146	0.11337	0.00022	2.3	3.4
HB21	1.69	0.281	1.82	0.744	0.11355	0.00005	2.2	-3.1
HB22	1.09	0.094	1.33	0.339	0.11688	0.00071	1.8	8.4
HB23	1.05	0.032	2.27	0.068	0.11422	0.00003	2.1	2.5
HB32	1.44	0.046	2.11	0.105	0.11318	0.00002	2.3	3.0
HB44		0.012	0.26	0.218	0.11323	0.00038	2.3	4.6

depletion ages (T_{RD}) calculated relative to the primitive upper mantle (PUM; (Meisel et al., 2001)) vary from the Paleoproterozoic to Late Archean (1.8–2.6 Ga) and are younger than the T_{RD} of the sulfides (2.7–3.2 Ga). The model ages (T_{MA}) of both HB21 and HB44 are older than the Earth's age, whereas sample HB21 gives a negative T_{MA} . These meaningless T_{MA} clearly indicate the disturbance of the Re–Os isotope systematics in these three samples. Other samples give potentially meaningful T_{MA} of 2.3–3.4 Ga, but disturbance of the Re–Os system in these samples is also likely. The low-Fo sample HB32 has T_{RD} and T_{MA} ages similar to the high-Fo samples.

4.5. Clinopyroxene Sr isotopes

Clinopyroxenes in thirteen samples with high Sr contents (>399 ppm) have been measured for Sr isotopes by laser ablation method, and the results are listed in Table 6. Clinopyroxene in each sample has been analyzed at 9–17 points, depending on grain size. After correction for fractionation and interferences, both $^{84}\text{Sr}/^{86}\text{Sr}$ and $^{84}\text{Sr}/^{88}\text{Sr}$ ratios display limited variation (0.0559–0.0578 vs. 0.0068–0.0069, respectively), and are identical to the accepted values of natural Sr isotopes (0.0565 vs. 0.00675, respectively). Clinopyroxenes in most samples have low Rb contents with $^{87}\text{Rb}/^{86}\text{Sr}$ ratios of 0.0002–0.0153, which is typical of mantle diopside (Pearson et al., 2003). Clinopyroxene in sample HB35 contains somewhat more Rb with an $^{87}\text{Rb}/^{86}\text{Sr}$ ratio of 0.0742. The $^{87}\text{Sr}/^{88}\text{Sr}$ ratios vary from 0.70309 to 0.70556, which are remarkably lower than whole-rock values of mantle xenoliths entrained in the Paleozoic kimberlites in the NCC (Zheng, 1999; Wu et al., 2006). The standard errors for all samples (0.00007–0.00033) are variably higher than the estimated external reproducibility of 0.00005 for the method (Yang et al., 2009a,b), which is probably due to their variable Rb contents. In particular, clinopyroxene in HB35 has the highest Rb content and the largest error. On the other hand, it might also reflect isotopic heterogeneity within the single grains (Schmidberger et al., 2003).

5. Discussion

5.1. Age and nature of the Hebi mantle xenoliths

Various studies have used the Re–Os isotopes of mantle xenoliths from the NCC to constrain the age of the lithospheric mantle at different times (Gao et al., 2002; Wu et al., 2003, 2006; Xu et al., 2008; Zhang et al., 2008; Chu et al., 2009; Zhang et al., 2009; Liu et al., 2010b). Mantle xenoliths entrained in the Paleozoic kimberlites (i.e., Mengyin, Fuxian and Tieling) have unradiogenic $^{187}\text{Os}/^{188}\text{Os}$ ratios varying from 0.10629 to 0.12220, which give Re depletion ages (T_{RD}) up to ca 3 Ga (Gao et al., 2002; Wu et al., 2006; Zhang et al., 2008; Chu et al., 2009). This supports the existence of Archean mantle along the eastern edge of the NCC during the Paleozoic (Gao et al., 2002; Wu et al., 2006; Zhang et al., 2008; Chu et al., 2009).

Table 6
Sr isotopes of clinopyroxenes in Hebi mantle xenoliths in-situ determined by LA-MC-ICPMS. T: temperatures calculated by Ca-in-opx geothermometer (Brey and Kohler, 1990).

	T (°C)	Fo in Ol	Cr# in Sp	Sr (ppm)	⁸⁸ Sr (V)	⁸⁵ Rb (V)	⁸⁷ Rb/ ⁸⁶ Sr	⁸⁷ Sr/ ⁸⁶ Sr	⁸⁴ Sr/ ⁸⁶ Sr	⁸⁴ Sr/ ⁸⁸ Sr
HB01	1050	92.5	0.52	389	2.10	0.00014	0.00023	0.70556 ± 16	0.0578 ± 2	0.00691 ± 3
HB07	1049	92.5	0.45	478	4.24	0.00020	0.00023	0.70431 ± 23	0.0570 ± 2	0.00681 ± 3
HB09	1051	92.0	0.43	403	1.98	0.00642	0.00290	0.70351 ± 10	0.0577 ± 1	0.00689 ± 1
HB10	1034	92.1	0.28	595	2.73	0.00492	0.00591	0.70499 ± 10	0.0571 ± 2	0.00681 ± 2
HB18	1020	92.2	0.45	474	2.66	0.00035	0.00042	0.70465 ± 07	0.0575 ± 2	0.00686 ± 2
HB20	1056	91.8	0.52	449	0.70	0.00148	0.00650	0.70323 ± 10	0.0567 ± 4	0.00677 ± 5
HB35	985	92.0	0.35	516	0.77	0.01986	0.07418	0.70430 ± 33	0.0561 ± 4	0.00670 ± 5
HB36	1059	91.8		407	0.69	0.00118	0.00544	0.70315 ± 7	0.0560 ± 4	0.00668 ± 5
HB39	1055	91.7	0.48	519	0.84	0.00007	0.00028	0.70321 ± 8	0.0560 ± 3	0.00669 ± 4
HB43	1037	91.2	0.59	402	0.75	0.00256	0.01202	0.70408 ± 18	0.0565 ± 5	0.00674 ± 6
HB44	1031	91.7	0.49	592	0.77	0.00477	0.01532	0.70473 ± 5	0.0563 ± 3	0.00672 ± 3
HB50	1044	91.6	0.50	481	0.61	0.00088	0.00490	0.70309 ± 9	0.0559 ± 4	0.00667 ± 5
HB62	1042	91.7	0.49	947	0.96	0.00044	0.00150	0.70548 ± 5	0.0565 ± 5	0.00674 ± 6

In contrast, mantle xenoliths entrained by the Cenozoic basalts have ¹⁸⁷Os/¹⁸⁸Os ratios remarkably higher than those of Paleozoic xenoliths (Gao et al., 2002; Wu et al., 2003, 2006; Xu et al., 2008; Zhang et al., 2008; Chu et al., 2009; Zhang et al., 2009; Liu et al., 2010b). Furthermore, Cenozoic mantle xenoliths from the western NCC have lower ¹⁸⁷Os/¹⁸⁸Os values than those from the eastern NCC (Gao et al., 2002; Wu et al., 2003, 2006; Xu et al., 2008; Zhang et al., 2008; Chu et al., 2009; Zhang et al., 2009; Liu et al., 2010b). Mantle xenoliths carried by Cenozoic basalts in the eastern NCC show a distribution of ¹⁸⁷Os/¹⁸⁸Os very similar to that of the convective upper mantle (see Fig. 11 in Chu et al., 2009), in which ancient mantle domains can be preserved through the convective stirring (Liu et al., 2008). This suggests that the old lithospheric mantle beneath the eastern NCC might have been completely removed and replaced by juvenile mantle accreted from the asthenosphere (Chu et al., 2009). In comparison, Cenozoic mantle xenoliths from the western NCC (i.e., Yangyuan, Fansi and Hannuoba) have less radiogenic ¹⁸⁷Os/¹⁸⁸Os ratios, with the lowest value of 0.110 (Gao et al., 2002; Xu et al., 2008; Liu et al., 2010b, 2011b). This indicates the preservation of Archean and Proterozoic mantle relics beneath the western NCC during the Cenozoic (Gao et al., 2002; Xu et al., 2008; Liu et al., 2010b, 2011b).

The analyzed Hebi mantle xenoliths have unradiogenic ¹⁸⁷Os/¹⁸⁸Os ratios ranging from 0.11067 to 0.11688 (Fig. 7). Their bulk-rock ¹⁸⁷Os/¹⁸⁸Os ratios give T_{RD} ages varying from Paleoproterozoic to Neoproterozoic (1.8–2.6 Ga), which is slightly younger than the previous reported T_{RD} ages of two sulfide grains (2.5 and 3.0 Ga) in Hebi mantle xenoliths (Zheng et al., 2007). Nevertheless, bulk-rock Re–Os isotopes of the Hebi mantle xenoliths give T_{MA} ages similar

to those given by sulfides, i.e., 2.3–3.4 Ga vs 2.5–3.0 Ga. It should be emphasized that the T_{RD} age, which assumes no Re is left in the residual peridotite after melting, represents the minimum age of melting experienced by mantle peridotites (Walker et al., 1989). In contrast, the model age (T_{MA}), which is calculated using the measured Re/Os ratio, represents the maximum age of the putative melting events, assuming that the Re/Os ratio has remained unchanged. Therefore, the bulk-rock Re–Os isotopes of Hebi mantle xenoliths are consistent with their derivation from the Archean lithospheric mantle, which has remained in this region after the lithospheric thinning.

The refractory chemical compositions of the Hebi mantle xenoliths are also consistent with the inference that they represent Archean cratonic mantle relics. The Hebi mantle xenoliths have high bulk-rock contents of MgO but low contents of CaO, Al₂O₃ and TiO₂, reflecting the loss of large proportions of basaltic components (Fig. 2a, b). The low Al₂O₃ contents of the Hebi mantle xenoliths indicate that they might represent residues of a fertile mantle after 15–35% equilibrium partial melting at pressure of 2 GPa (Fig. 2b). Olivines in most Hebi mantle xenoliths have Fo contents of 91–93 and spinels are commonly Cr-rich. The degrees of partial melting estimated from spinel Cr# suggest that the Hebi mantle xenoliths have been subjected to 11–19% fractional melting. The refractory characteristics shown by the Hebi mantle xenoliths are in stark contrast to the Cenozoic mantle xenoliths from the eastern NCC, which are dominated by spinel lherzolites with fertile compositions (Gao et al., 2002; Rudnick et al., 2004; Wu et al., 2006; Zheng et al., 2006; Chu et al., 2009).

Besides the high-Fo mantle xenoliths, the Hebi basalts also contain a minor population of xenoliths with low-Fo olivines (Zheng et al., 2001). The low-Fo xenoliths have fertile compositions, which has been explained as juvenile mantle that was newly accreted from the asthenosphere underneath the refractory mantle relic (Zheng et al., 2001). However, the ¹⁸⁷Os/¹⁸⁸Os ratio of the only analyzed low-Fo xenolith (HB-32) is indistinguishable from the high-Fo harzburgites, and also gives an Archean model age. In a recent study, a Hebi mantle xenolith with low-Fo content (Fo = 89.6) also gave an unradiogenic ¹⁸⁷Os/¹⁸⁸Os ratio of 0.1125 and an old model age of 2.2 Ga (Liu et al., 2011b). The ancient model age is incompatible with the idea of accreted juvenile mantle. Therefore, we suggest that the low-Fo xenoliths might also represent the Archean mantle, but have been subjected to recent melt refertilization.

Garnet is absent in the Hebi mantle xenoliths, pointing to a thin lithospheric mantle remained in this area during the Cenozoic (Zheng et al., 2001). This implies that the thick Archean cratonic mantle has been significantly thinned (Zheng et al., 2001). On the other hand, most Hebi mantle xenoliths have equilibrium temperatures higher than 1000 °C (Fig. 6). This suggests that the mantle relic was heated by the upwelling of hot asthenosphere, which was triggered by the lithospheric thinning.

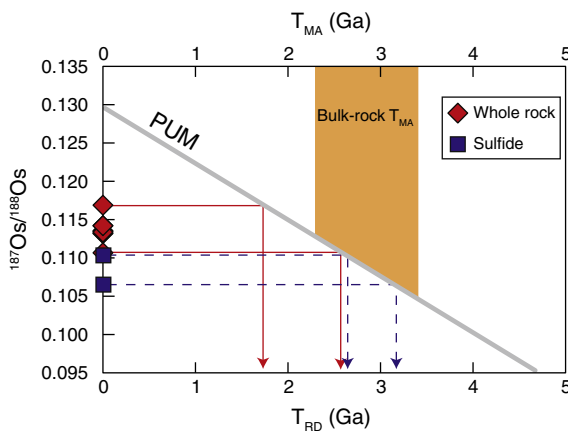


Fig. 7. T_{RD} and T_{MA} ages of the Hebi mantle xenoliths. The T_{RD} ages of two sulfide grains from Hebi mantle xenoliths reported by Zheng et al. (2007) are also shown for comparison.

5.2. Sr isotopes of clinopyroxenes in Hebi mantle xenoliths

The $^{87}\text{Sr}/^{86}\text{Sr}$ ratios of clinopyroxenes in thirteen Hebi mantle xenoliths range from 0.70309 to 0.70556 (Fig. 8a), which are similar to the reported values (0.70205–0.70489) of clinopyroxene in Cenozoic mantle xenoliths from the eastern NCC obtained by solution method (Fig. 8b). This indicates that the Archean mantle relic beneath Hebi has depleted to weakly enriched Sr isotopic characteristics. In contrast, mantle xenoliths entrained in the Paleozoic kimberlites (i.e., Mengyin and Tieling) have more radiogenic $^{87}\text{Sr}/^{86}\text{Sr}$ ratios of 0.7039–0.7140 (Fig. 8c), suggesting that the Archean cratonic mantle might have Sr-isotope compositions enriched in ^{87}Sr (Zheng, 1999; Wu et al., 2006). Before we discuss the difference in Sr isotopes between the Hebi mantle xenoliths and the Paleozoic mantle xenoliths, it is necessary to evaluate the effects of contamination by the host basalts and kimberlites.

Using the laser-ablation method, Schmidberger et al. (2003) showed that clinopyroxene in mantle xenoliths from the Nikos kimberlite in the northern Canadian Craton record intra- and inter-sample Sr-isotope heterogeneity. The authors have ascribed the

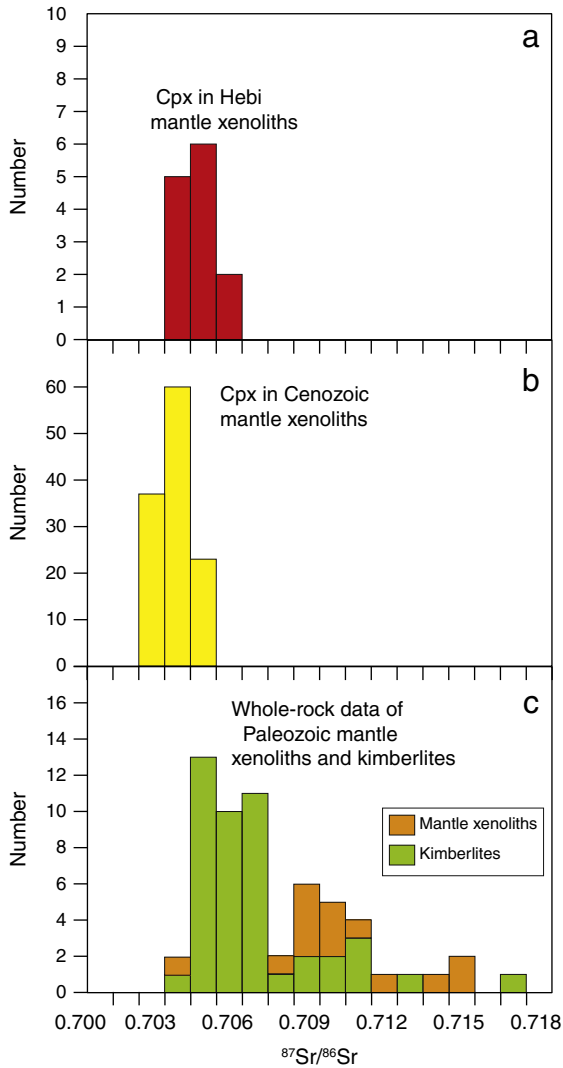


Fig. 8. Histogram of $^{87}\text{Sr}/^{86}\text{Sr}$ ratios. (a) Whole-rock $^{87}\text{Sr}/^{86}\text{Sr}$ ratios of the Paleozoic kimberlites (Zhang and Yang, 2007; Yang et al., 2009a) and the entrained mantle xenoliths (Zheng, 1999; Wu et al., 2006). (b) $^{87}\text{Sr}/^{86}\text{Sr}$ ratios of clinopyroxenes in Hebi mantle xenoliths by LA-MC-ICPMS. (c) $^{87}\text{Sr}/^{86}\text{Sr}$ ratios of clinopyroxenes in Cenozoic mantle xenoliths from the NCC (Song and Frey, 1989; Xu et al., 1998; Rudnick et al., 2004; Xu et al., 2004; Ma and Xu, 2006; Wu et al., 2006; Xu et al., 2008; Chu et al., 2009).

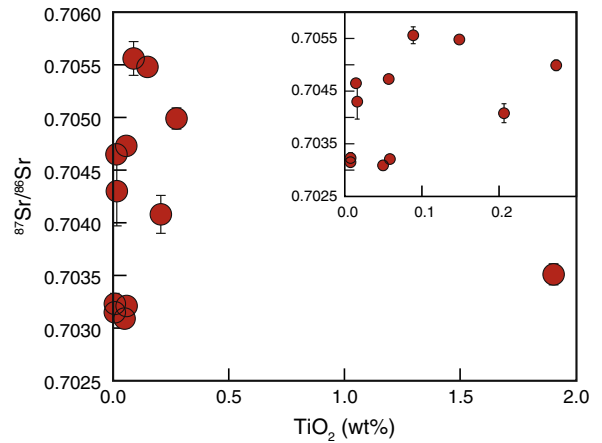


Fig. 9. $^{87}\text{Sr}/^{86}\text{Sr}$ vs. TiO_2 in clinopyroxene from the Hebi xenoliths. The error bar is 26 (SE).

radiogenic Sr isotopes to the metasomatic interaction with the host kimberlites, which have higher Sr contents than clinopyroxene (i.e., 1000–2200 ppm vs. 100–400 ppm). However, such a mechanism cannot be applied to explain unradiogenic Sr isotopes of the Hebi clinopyroxenes. First, the Hebi clinopyroxene with Sr isotope analyses have Sr contents close to or slightly lower than the Cenozoic basalts in Taihang Mountain areas (central NCC), i.e. 389–974 ppm vs. 277–1290 ppm (Xu et al., 2004; Tang et al., 2006). Secondly, there is a large difference in TiO_2 concentration between clinopyroxene and the host basalt. Therefore, the most unradiogenic $^{87}\text{Sr}/^{86}\text{Sr}$ ratios would be recorded by clinopyroxene that had experienced the largest degree metasomatic interaction with the host basalt, which should also have the highest TiO_2 content. That is, a negative correlation is expected between the clinopyroxene $^{87}\text{Sr}/^{86}\text{Sr}$ ratios and TiO_2 contents. However, the Hebi clinopyroxenes show a positive $^{87}\text{Sr}/^{86}\text{Sr}$ – TiO_2 relationship (Fig. 9). Except for sample HB09, clinopyroxene with unradiogenic $^{87}\text{Sr}/^{86}\text{Sr}$ ratios also have low TiO_2 contents. This suggests that the unradiogenic Sr isotopes of clinopyroxenes in the Hebi mantle xenoliths did not result from interaction with the host basalt. Therefore, the depleted Sr isotope compositions of the Hebi clinopyroxene were established prior to entrainment in the host basalt.

5.3. Metasomatic origin of clinopyroxene in the Hebi mantle xenoliths

The trace-element compositions of clinopyroxenes in the Hebi mantle xenoliths show variably enriched characteristics, which are inconsistent with a residual origin. The clinopyroxenes have strongly fractionated REE patterns, with enrichment of LREE over HREE (Fig. 5a, c). They also show enrichment in LILE (e.g., Ba, Th and U) but pronounced negative anomalies in HFSE (e.g., Zr, Hf, Nb, Ta and Ti; Fig. 5b, d). This would indicate that the clinopyroxene has a metasomatic origin or at the very least has been overprinted by a metasomatic event. Various metasomatic agents have been proposed to account for the observed incompatible-element features and mineralogy in mantle xenoliths, including silicate melts (Zangana et al., 1999), hydrous (Downes, 2001; Liu et al., 2011a) or CO_2 -rich fluids (O'Reilly and Griffin, 1988), and carbonatitic melts (Rudnick et al., 1993; Ionov et al., 1997; Yaxley et al., 1998; Coltorti et al., 1999; Malarkey et al., 2011). It has been suggested that mantle xenoliths metasomatized by carbonatite melts would be more enriched in LREE but depleted in HFSE (e.g., Ti and Zr) than those affected by silicate melts (Coltorti et al., 1999). The negative anomaly for HFSE (in particular Zr and Hf) in the multi-element plots is indicative of clinopyroxene that has crystallized from, or re-equilibrated with, a carbonate melt (Coltorti et al., 1999; Blundy and Dalton, 2000).

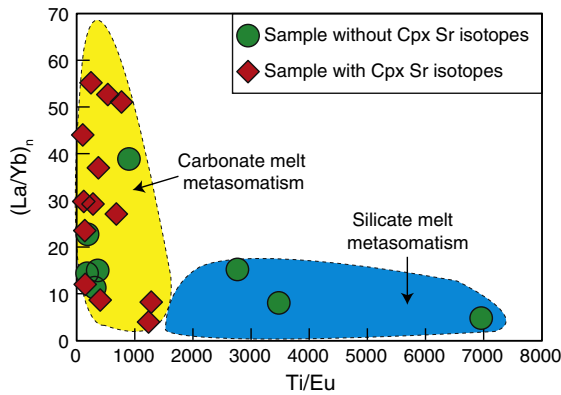


Fig. 10. $(La/Yb)_n$ vs. Ti/Eu ratios of clinopyroxene in the Hebi mantle xenoliths. Data are primitive-mantle normalized (McDonough and Sun, 1995). Areas of carbonate and silicate melt metasomatism are from Coltorti et al. (1999).

Clinopyroxenes in most Hebi mantle xenoliths have high La/Yb but low Ti/Eu ratios, which are consistent with metasomatism by carbonate melts (Fig. 10). Carbonate metasomatism has been previously proposed to account for the enriched trace element features in Hebi mantle xenoliths (Zheng et al., 2001). Nevertheless, three Hebi samples plot into the area defined by silicate melt metasomatism. This suggests that the lithospheric mantle beneath Hebi has been metasomatized by more than one metasomatic agent.

All Hebi mantle xenoliths with in-situ determination of clinopyroxene Sr isotopes plot in the area of carbonate melt metasomatism (Fig. 10). Therefore, the Sr isotopes of clinopyroxene in these samples do not mean that the Archean lithospheric mantle beneath the NCC has an unradiogenic Sr isotope composition, but result from metasomatic processes. The limited variation in $^{87}Sr/^{86}Sr$ of clinopyroxene in the Hebi peridotites is inconsistent with long-term enrichment. However, it is not possible to accurately date the clinopyroxene addition and thus melt metasomatism using the Rb–Sr isochron method. The Hebi clinopyroxenes have a limited range in Rb/Sr ratios, and the Rb–Sr isotope data from the Hebi clinopyroxene do not show an isochronous relationship. This suggests that the range in clinopyroxene $^{87}Sr/^{86}Sr$ is not generated by radiogenic ingrowth but probably is due to the result of complex metasomatic interactions, which has been inferred for the majority of mantle clinopyroxene Rb/Sr isotope data from off-craton SCLM (Pearson et al., 2003). We suggest that the mildly unradiogenic Sr-isotope compositions of the Hebi mantle xenoliths resulted from a recent crystallization or re-equilibration with carbonatitic melts.

Therefore, the Sr isotope compositions of the Archean cratonic mantle beneath the NCC cannot be constrained by the Hebi mantle xenoliths, although Re–Os isotopes indicate that they represent an Archean mantle relic. The Archean cratonic mantle might have enriched Sr isotope compositions, as recorded by the Paleozoic mantle xenoliths (Zheng, 1999; Wu et al., 2006). However, the possibility that the radiogenic Sr isotopes resulting from the alteration and contamination (from the kimberlite) experienced by these rocks cannot be eliminated.

5.4. Effects of clinopyroxene addition on the Os model ages

Various studies have suggested that clinopyroxene addition is common in mantle xenoliths from both on-craton (van Achterbergh et al., 2001; Gregoire et al., 2003; Pearson et al., 2003; Simon et al., 2003, 2007) and off-craton localities (Malarkey et al., 2011). Addition of clinopyroxene accompanying the metasomatic processes would result in the refractory lithospheric mantle becoming fertile, i.e., refertilization (Saal et al., 2001; Le Roux et al., 2007; Van Acken et al., 2008). It has been suggested that addition of sulfides along

with refertilization processes would increase the $^{187}Os/^{188}Os$ ratios and thus decrease the Os model ages of mantle peridotites, i.e., rejuvenation (Becker et al., 2001; Saal et al., 2001; Beyer et al., 2006; Van Acken et al., 2008; Zhang et al., 2009), as the secondary sulfides commonly have radiogenic Os isotopes relative to the primary ones (Alard et al., 2002, 2005).

Although the rocks have experienced clinopyroxene addition, the bulk-rock $^{187}Os/^{188}Os$ ratios of the Hebi mantle xenoliths are still unradiogenic (0.11067–0.11688), and give Paleoproterozoic–Neoproterozoic T_{RD} ages (1.8–2.6 Ga) and T_{MA} ages (2.3–3.4 Ga). The bulk-rock T_{MA} ages are very similar to the T_{MA} ages given by the sulfides (2.5–3.0 Ga) in the Hebi mantle xenoliths (Zheng et al., 2007). This suggests that melt refertilization (i.e., clinopyroxene addition) had little effect on the Re–Os isotopes of the Hebi mantle xenoliths. The reason might be that little sulfide has been added from the refertilizing melts or that the added secondary sulfides had low Os contents, and played an insignificant role in the whole-rock Os budget (Alard et al., 2000). On the other hand, addition of clinopyroxene also does not significantly increase the Re content, due to the low modal contents of clinopyroxene in the Hebi mantle xenoliths.

6. Conclusions

The Hebi mantle xenoliths have refractory compositions and old Os model ages, indicating that they represent an Archean cratonic mantle relic. This suggests that the lithospheric mantle beneath the NCC has been heterogeneously thinned and removed. Clinopyroxene in the Hebi mantle xenoliths shows strong enrichment in LILE but variable depletion in HFSE, which do not favor a residual origin. The Hebi clinopyroxene might be crystallized from a recent carbonatitic metasomatic event. The depleted to weakly enriched $^{87}Sr/^{86}Sr$ ratios of clinopyroxene in the Hebi mantle xenoliths thus do not reflect the isotopic compositions of the Archean cratonic mantle beneath the NCC. The Re–Os isotope systems of the Hebi mantle xenoliths have not been significantly disturbed by the clinopyroxene addition processes.

Acknowledgements

This study was supported by the funds from Chinese Academy of Sciences (KZCX2-EW-109) and National Natural Science Foundation of China (No. 40873024). We thank Bo Wan and Hua-Feng Qin for sample collection in the field; Qian Mao and Yu-Guang Ma for help in the electron probe experiment. W.L. Griffin kindly improved the language of the final version.

References

- Alard, O., Griffin, W.L., Lorand, J.P., Jackson, S.E., O'Reilly, S.Y., 2000. Non-chondritic distribution of the highly siderophile elements in mantle sulphides. *Nature* 336, 665–667.
- Alard, O., Griffin, W.L., Pearson, N.J., Lorand, J.P., O'Reilly, S.Y., 2002. New insights into the Re–Os systematics of sub-continental lithospheric mantle from in situ analysis of sulphides. *Earth and Planetary Science Letters* 203, 651–663.
- Alard, O., Lugeat, A., Pearson, N.J., Griffin, W.L., Lorand, J.P., Bannoun, A., Burton, K.W., O'Reilly, S.Y., 2005. In-situ Os isotopes in abyssal peridotites bridge the isotopic gap between MORB and their source mantle. *Nature* 436, 1005–1008.
- Anders, E., Grevesse, N., 1989. Abundances of the elements – meteoritic and solar. *Geochimica et Cosmochimica Acta* 53, 197–214.
- Becker, H., Shirey, S.B., Carlson, R.W., 2001. Effects of melt percolation on the Re–Os systematics of peridotites from a Paleozoic convergent plate margin. *Earth and Planetary Science Letters* 188, 107–121.
- Beyer, E.E., Griffin, W.L., O'Reilly, S.Y., 2006. Transformation of archaean lithospheric mantle by refertilization: evidence from exposed peridotites in the Western Gneiss Region, Norway. *Journal of Petrology* 47, 1611–1636.
- Blundy, J., Dalton, J., 2000. Experimental comparison of trace element partitioning between clinopyroxene and melt in carbonate and silicate systems, and implications for mantle metasomatism. *Contributions to Mineralogy and Petrology* 139, 356–371.

- Boyd, F.R., Pokhilenko, N.P., Pearson, D.G., Mertzman, S.A., Sobolev, N.V., Finger, L.W., 1997. Composition of the Siberian cratonic mantle: evidence from Udachnaya peridotite xenoliths. *Contributions to Mineralogy and Petrology* 128, 228–246.
- Brey, G.P., Kohler, T., 1990. Geothermobarometry in four-phase lherzolites II. new thermobarometers, and practical assessment of existing thermobarometers. *Journal of Petrology* 31, 1353–1378.
- Chu, Z.Y., Wu, F.Y., Walker, R.J., Rudnick, R.L., Pitcher, L., Puchtel, L.S., Yang, Y.H., Wilde, S.A., 2009. Temporal evolution of the lithospheric mantle beneath the Eastern North China Craton. *Journal of Petrology* 50, 1857–1898.
- Coltorti, M., Bonadiman, C., Hinton, R.W., Siena, F., Upton, B.G.J., 1999. Carbonatite metasomatism of the oceanic upper mantle: evidence from clinopyroxenes and glasses in ultramafic xenoliths of Grande Comore, Indian Ocean. *Journal of Petrology* 40, 133–165.
- Dobbs, P.N., Duncan, D.J., Hu, S., Shee, S.R., Colgan, E.A., Brown, M.A., Smith, C.B., Allsopp, H.P., 1994. The geology of Mengyin kimberlites, Shandong, China. In: Meyer, O.A., Leonardos, O.H. (Eds.), *Kimberlites, Related Rocks and Mantle Xenoliths*. CPRM, Spec. pp. 40–61.
- Downes, H., 2001. Formation and modification of the shallow sub-continental lithospheric mantle: a review of geochemical evidence from ultramafic xenoliths suites and tectonically emplaced ultramafic massifs of western and central Europe. *Journal of Petrology* 42, 233–250.
- Gao, S., Rudnick, R.L., Carlson, R.W., McDonough, W.F., Liu, Y.S., 2002. Re–Os evidence for replacement of ancient mantle lithosphere beneath the North China craton. *Earth and Planetary Science Letters* 198, 307–322.
- Gregoire, M., Bell, D.R., Le Roux, A.P., 2003. Garnet lherzolites from the Kaapvaal craton (South Africa): trace element evidence for a metasomatic history. *Journal of Petrology* 44, 629–657.
- Griffin, W.L., Zhang, A.D., O'Reilly, S.Y., Ryan, C.G., 1998. Phanerozoic evolution of the lithosphere beneath the Sino-Korean craton. In: Flower, M.F.J., Chung, S.L., Lo, C.H., Lee, T.Y. (Eds.), *Mantle Dynamics and Plate Interactions in East Asia, Geodynamic Series*. American Geophysical Union, Washington D. C., pp. 107–126.
- Hellebrand, E., Snow, J.E., Dick, H.J.B., Hofmann, A.W., 2001. Coupled major and trace elements as indicators of the extent of melting in mid-ocean-ridge peridotites. *Nature* 410, 677–681.
- Herzberg, C., 2004. Geodynamic information in peridotite petrology. *Journal of Petrology* 45, 2507–2530.
- Ionov, D.A., Griffin, W.L., O'Reilly, S.Y., 1997. Volatile-bearing minerals and lithophile trace elements in the upper mantle. *Chemical Geology* 141, 153–184.
- Le Roux, V., Bodinier, J.L., Tommasi, A., Alard, O., Dautria, J.M., Vauchez, A., Riches, A.J.V., 2007. The Lherz spinel lherzolite: refertilized rather than pristine mantle. *Earth and Planetary Science Letters* 259, 599–612.
- Liu, R.X., Chen, W., Sun, J., Li, D., 1990. The K–Ar age and tectonic environment of Cenozoic volcanic rock in China. In: Liu, R.X. (Ed.), *The Age and Geochemistry of Cenozoic Volcanic Rock in China*. Seismology Published House, Beijing, pp. 1–43.
- Liu, C.Z., Snow, J.E., Hellebrand, E., Bruggmann, G., von der Handt, A., Buchl, A., Hofmann, A.W., 2008. Ancient, highly heterogeneous mantle beneath Gakkel ridge, Arctic Ocean. *Nature* 452, 311–316.
- Liu, C.Z., Wu, F.Y., Wilde, S.A., Yu, L.J., Li, J.L., 2010a. Anorthitic plagioclase and pargasitic amphibole in mantle peridotites from Yungbwa ophiolite (southern Tibetan Plateau) formed by hydrous melt metasomatism. *Lithos* 114, 413–422.
- Liu, J.G., Rudnick, R.L., Walker, R.J., Gao, S., Wu, F.Y., Piccoli, P.M., 2010b. Processes controlling highly siderophile element fractionations in xenolithic peridotites and their influence on Os isotopes. *Earth and Planetary Science Letters* 297, 287–297.
- Liu, C.Z., Wu, F.Y., Chung, S.L., Zhao, Z.D., 2011a. Fragments of hot and metasomatized mantle lithosphere in Middle Miocene ultrapotassic lavas, southern Tibet. *Geology* 39, 923–926.
- Liu, J.G., Rudnick, R.L., Walker, R.J., Gao, S., Wu, F.Y., Piccoli, P.M., Yuan, H.L., Xu, W.L., Xu, Y.G., 2011b. Mapping lithospheric boundaries using Os isotopes of mantle xenoliths: an example from the North China Craton. *Geochimica et Cosmochimica Acta* 75, 3881–3902.
- Lu, F.X., Zheng, J.P., 1996. Characteristics of Paleozoic lithosphere and deep processes in the North China platform. In: Chi, J.S., Lu, F.X. (Eds.), *Characteristics of Kimberlites and Paleozoic Lithosphere in the North China Platform*. Science Press, Beijing, pp. 215–274.
- Ma, J.L., Xu, Y.G., 2006. Old EMI-type enriched mantle under the middle North China Craton as indicated by Sr and Nd isotopes of mantle xenoliths from Yangyuan, Hebei Province Chinese Science Bulletin 51, 1343–1349.
- Malarkey, J., Wittig, N., Pearson, D.G., Davidson, J.P., 2011. Characterising modal metasomatic processes in young continental lithospheric mantle: a microsampling isotopic and trace element study on xenoliths from the Middle Atlas Mountains, Morocco. *Contributions to Mineralogy and Petrology* 162, 289–302.
- McDonough, W.F., Sun, S.S., 1995. The composition of the Earth. *Chemical Geology* 120, 223–253.
- McFarlane, C., McCulloch, M., 2008. Sm–Nd and Sr isotope systematics in LREE-rich accessory minerals using LA–MC–ICP–MS. In: Sylvester, P. (Ed.), *Laser Ablation–ICPMS in the Earth Sciences*. Mineralogical Association of Canada Short Course, Vancouver, B.C., pp. 117–133.
- Meisel, T., Walker, R.J., Irving, A.J., Lorand, J.P., 2001. Osmium isotopic compositions of mantle xenoliths: a global perspective. *Geochimica et Cosmochimica Acta* 65, 1311–1323.
- Menzies, M.A., Hawkesworth, C.J., 1987. *Mantle Metasomatism*. Academic Press, London, p. 472.
- O'Reilly, S.Y., Griffin, W.L., 1988. Mantle metasomatism beneath western Victoria, Australia: I. Metasomatic processes in Cr–diopside lherzolites. *Geochimica et Cosmochimica Acta* 52, 433–447.
- Pearson, D.G., Canil, D., Shirey, S.B., 2003. Mantle sample included in volcanic rocks: xenoliths and diamonds. In: Carlson, R.W. (Ed.), *Treatise on geochemistry: the mantle and core*. Elsevier, Amsterdam, pp. 171–276.
- Ramos, F.C., Wolff, J.A., Tollstrup, D.L., 2004. Measuring $^{87}\text{Sr}/^{86}\text{Sr}$ variations in minerals and groundmass from basalts using LA–MC–ICPMS. *Chemical Geology* 211, 135–158.
- Rudnick, R.L., McDonough, W.F., Chappell, B.W., 1993. Carbonatite metasomatism in the northern Tanzanian mantle: petrographic and geochemical characteristics. *Earth and Planetary Science Letters* 114, 463–475.
- Rudnick, R.L., Gao, S., Ling, W.L., Liu, Y.S., McDonough, W.F., 2004. Petrology and geochemistry of spinel peridotite xenoliths from Hannuoba and Qixia, North China craton. *Lithos* 77, 609–637.
- Saal, A.E., Takazawa, E., Frey, F.A., Shimizu, N., Hart, S.R., 2001. Re–Os isotopes in the Horoman peridotite: evidence for refertilization? *Journal of Petrology* 42, 25–37.
- Schmidberger, S.S., Simonetti, A., Francis, D., 2003. Small-scale Sr isotope investigation of clinopyroxenes from peridotite xenoliths by laser ablation MC–ICP–MS—implications for melt metasomatism. *Chemical Geology* 199, 317–329.
- Simon, N.S.C., Irvine, G.J., Davies, G.R., Pearson, D.G., Carlson, R.W., 2003. The origin of garnet and clinopyroxene in “depleted” Kaapvaal peridotites. *Lithos* 71, 289–322.
- Simon, N.S.C., Carlson, R.W., Pearson, D.G., Davies, G.R., 2007. The origin and evolution of the Kaapvaal cratonic lithospheric mantle. *Journal of Petrology* 48, 589–625.
- Song, Y., Frey, F.A., 1989. Geochemistry of peridotite xenoliths in basalt from Hannuoba, Eastern China: implications for subcontinental mantle heterogeneity. *Geochimica et Cosmochimica Acta* 53, 97–113.
- Tang, Y.J., Zhang, H.F., Ying, J.F., 2006. Asthenosphere–lithospheric mantle interaction in an extensional regime: implication from the geochemistry of Cenozoic basalts from Taihang Mountains, North China Craton. *Chemical Geology* 233, 309–327.
- van Achen, D., Becker, H., Walker, R.J., 2008. Refertilization of Jurassic oceanic peridotites from the Tethys Ocean – implications for the Re–Os systematics of the upper mantle. *Earth and Planetary Science Letters* 268, 171–181.
- Walker, R.J., Shirey, S.B., Hanson, G.N., Rajamani, V., Horan, M.F., 1989. Re–Os, Rb–Sr, and O isotopic systematics of the Archean Kolar schist belt, Karnataka, India. *Geochimica et Cosmochimica Acta* 53, 3005–3013.
- Wells, P.R.A., 1977. Pyroxene thermometry in simple and complex systems. *Contributions to Mineralogy and Petrology* 62, 129–139.
- Witt-Eickchen, G., Seck, H.A., 1991. Solubility of Ca and Al in orthopyroxene from spinel peridotite: an improved version of an empirical geothermometer. *Contributions to Mineralogy and Petrology* 106, 431–439.
- Wu, F.Y., Walker, R.J., Ren, X.W., Sun, D.Y., Zhou, X.H., 2003. Osmium isotopic constraints on the age of lithospheric mantle beneath northeastern China. *Chemical Geology* 196, 107–129.
- Wu, F.Y., Lin, J.Q., Wilde, S.A., Zhang, X., Yang, J.H., 2005. Nature and significance of the Early Cretaceous giant igneous event in eastern China. *Earth and Planetary Science Letters* 233, 103–119.
- Wu, F.Y., Walker, R.J., Yang, Y.H., Yuan, H.L., Yang, J.H., 2006. The chemical-temporal evolution of lithospheric mantle underlying the North China Craton. *Geochimica et Cosmochimica Acta* 70, 5013–5034.
- Xu, Y.G., 2007. Diachronous lithospheric thinning of the North China Craton and formation of the Daxin'anling–Taihangshan gravity lineament. *Lithos* 96, 281–298.
- Xu, Y.G., Menzies, M.A., Vroon, P., Mercier, J.C., Lin, C.Y., 1998. Texture-temperature-geochemistry relationships in the upper mantle as revealed from spinel peridotite xenoliths from Wangqing, NE China. *Journal of Petrology* 39, 469–493.
- Xu, Y.G., Chung, S.L., Ma, J.L., Shi, L.B., 2004. Contrasting Cenozoic lithospheric evolution and architecture in the western and eastern Sino-Korean Craton: constraints from geochemistry of basalts and mantle xenoliths. *Journal of Geology* 112, 593–605.
- Xu, Y.G., Blusztajn, J., Ma, J.L., Suzuki, K., Liu, J.F., Hart, S.R., 2008. Late Archean to Early Proterozoic lithospheric mantle beneath the western North China craton: Sr–Nd–Os isotopes of peridotite xenoliths from Yangyuan and Fansi. *Lithos* 102, 25–42.
- Yang, J.H., Wu, F.Y., Wilde, S.A., 2003. Geodynamic setting of large-scale Late Mesozoic gold mineralization in the North China Craton: an association with lithospheric thinning. *Ore Geology Review* 23, 125–152.
- Yang, Y.H., Wu, F.Y., Wilde, S.A., Liu, X.M., Zhang, Y.B., Xie, L.W., Yang, J.H., 2009a. In situ perovskite Sr–Nd isotopic constraints on the petrogenesis of the Ordovician Mengyin kimberlites in the North China Craton. *Chemical Geology* 264, 24–42.
- Yang, Y.H., Wu, F.Y., Xie, L.W., Yang, J.H., Zhang, Y.B., 2009b. In-situ Sr isotopic measurement of natural geological samples by LA–MC–ICP–MS. *Acta Petrologica Sinica* 25, 3431–3441 (in Chinese with English abstract).
- Yaxley, G.M., Green, D.H., Kamenetsky, V., 1998. Carbonatite Metasomatism in the Southeastern Australian Lithosphere. *Journal of Petrology* 39, 1917–1930.
- Zangana, N.A., Downes, H., Thirlwall, M.F., Marriner, G.F., Bea, F., 1999. Geochemical variation in peridotite xenoliths and their constituent clinopyroxenes from Ray Pic (French Massif Central): implications for the composition of the shallow lithospheric mantle. *Chemical Geology* 153, 11–35.
- Zhang, H.F., Yang, Y.H., 2007. Emplacement age and Sr–Nd–Hf isotopic characteristics of the diamondiferous kimberlites from the eastern North China Craton. *Acta Petrologica Sinica* 23, 285–294 (in Chinese with English abstract).
- Zhang, H.F., Goldstein, S.L., Zhou, X.H., Sun, M., Zheng, J.P., Cai, Y., 2008. Evolution of subcontinental lithospheric mantle beneath eastern China: Re–Os isotopic evidence from mantle xenoliths in Paleozoic kimberlites and Mesozoic basalts. *Contributions to Mineralogy and Petrology* 155, 271–293.
- Zhang, H.F., Goldstein, S.L., Zhou, X.H., Sun, M., Cai, Y., 2009. Comprehensive refertilization of lithospheric mantle beneath the North China Craton: further Os–Sr–Nd isotopic constraints. *Journal of the Geological Society* 166, 249–259.
- Zhao, G.C., Wilde, S.A., Cawood, P.A., Sun, M., 2001. Archean blocks and their boundaries in the North China Craton: lithological, geochemical, structural and P–T path constraints and tectonic evolution. *Precambrian Research* 107, 45–73.

- Zhao, X.M., Zhang, H.F., Zhu, X.K., Zhang, W.H., Yang, Y.H., Tang, Y.J., 2007. Metasomatism of Mesozoic and Cenozoic lithospheric mantle beneath the North China Craton: evidence from phlogopite-bearing mantle xenoliths. *Acta Petrologica Sinica* 23, 1281–1293 (in Chinese with English abstract).
- Zheng, J.P., 1999. Mesozoic-Cenozoic mantle replacement and lithospheric thinning, East China. China University of Geosciences Press, Wuhan, p. 126.
- Zheng, J.P., Lu, F.X., 1999. Petrologic characteristics of kimberlite-borne mantle xenoliths from the Shandong and Liaoning Peninsula: Paleozoic lithosphere mantle and its heterogeneity. *Acta Petrologica Sinica* 15, 65–74 (in Chinese with English abstract).
- Zheng, J.P., O'Reilly, S.Y., Griffin, W.L., Lu, F.X., Zhang, M., Pearson, N.J., 2001. Relict refractory mantle beneath the eastern North China block: significance for lithosphere evolution. *Lithos* 57, 43–66.
- Zheng, J.P., Griffin, W.L., O'Reilly, S.Y., Yang, J.S., Li, T.F., Zhang, M., Zhang, R.Y., Liou, J.G., 2006. Mineral chemistry of Peridotites from Paleozoic, Mesozoic and Cenozoic Lithosphere: constraints on mantle evolution beneath Eastern China. *Journal of Petrology* 47, 2233–2256.
- Zheng, J.P., Griffin, W.L., O'Reilly, S.Y., Yu, C.M., Zhang, H.F., Pearson, N., Zhang, M., 2007. Mechanism and timing of lithospheric modification and replacement beneath the eastern North China Craton: peridotitic xenoliths from the 100 Ma Fuxin basalts and a regional synthesis. *Geochimica et Cosmochimica Acta* 71, 5203–5225.